



# Integration of multi-scale porosimetry and multi-modal imaging in the study of structure-transport relationships in porous catalyst pellets

Suleiman Mousa<sup>a</sup>, Vladimir Novak<sup>b</sup>, Robin S. Fletcher<sup>c</sup>, Monica Garcia<sup>c</sup>, Norman Macleod<sup>c</sup>, Martin Corfield<sup>d</sup>, Sean P. Rigby<sup>a,\*</sup>

<sup>a</sup> Department of Chemical and Environmental Engineering, Faculty of Engineering, University of Nottingham, University Park, Nottingham NG7 2RD, UK

<sup>b</sup> Swiss Light Source, Paul Scherrer Institut, Forschungsstrasse 111, 5232 Villigen PSI, Switzerland

<sup>c</sup> Johnson Matthey, P.O. Box 1, Belasis Avenue, Billingham, Cleveland TS23 1LB, UK

<sup>d</sup> Faculty of Engineering, Power Electronics and Machines Centre, University of Nottingham, Jubilee Campus, Triumph Road, Nottingham NG7 2GA, UK

## ABSTRACT

The forming process for heterogeneous catalyst pellets impacts on reactor performance. In order to intelligently optimise the product formulation and manufacturing procedure, the impact of fabrication options on the resultant pore structure and mass transfer properties must be fully understood. In this work, the more direct information possible from multi-modal imaging methods has been combined with the more statistically-representative, multi-scale data from porosimetry, including the rarely-used gas overcondensation technique, to characterise batches of methanol synthesis catalyst tablets made using different feed types. Despite the hierarchies of complexity of the porous pellets revealed by the computerised X-ray tomography and FIB-SEM images, the impact on mass transfer of controlled modifications to the void space, achieved through mercury porosimetry, could be modelled using a relatively simple random pore-bond network. The characteristic parameters for the model were obtained from a percolation theory-based analysis of the overcondensation data. A quantitative relationship was thereby obtained between the structural information contained within the overcondensation isotherms and the rate of mass uptake of gas into the porous pellets. This revealed the differential importance to mass transfer of particular sets of pores, associated with certain pellet structural features, and the impact on tortuosity of pellet fabrication parameters such as particle feed size.

## 1. Introduction

The ultimate, observed activity of many heterogeneous catalysts, such as methanol synthesis pellets, is limited by mass transport rates, rather than the intrinsic reaction rate. The reaction rate is said to be diffusion-limited. In such cases, the effectiveness factor of the catalyst pellets is well below unity. For many industrial processes the effectiveness factor can be in the region of 50–60 % [1]. Hence, the performance efficiency of the catalytic process could be substantially improved by increasing catalyst effectiveness factor. This requires a deeper understanding of the pore structure-transport relationship within the catalyst pellets, and, also, how that pore structure depends upon the pellet fabrication method. In this work, we will study how different fabrication processes affect pore structure in the final pellet, and its impact on mass transport rates. In particular, how specific features of the void space are related to certain aspects of the fabrication process will be determined. This requires powerful pore structural characterisation methods that can deliver comprehensive and detailed analyses of the pellet void space.

In disordered porous media, heterogeneity often exists in the spatial

distribution of porosity over different length-scales, as illustrated in the schematic diagram in Figure A1 in the Supplementary Material. The void spaces themselves may also have varied characteristic sizes with different length-scales. Various imaging modalities such as atomic force microscopy (AFM), computerized X-ray tomography (CXT), scanning electron microscopy (FIB-SEM) and electron tomography (3D-TEM) have been used to directly study porous materials [2]. However, for materials with hierarchical or multi-scale porosity, no single imaging modality alone can visualise pores across all the size scales from nanopores to micron-sized macropores, or map macroscopic variation in nanoscopic properties [2–4]. Imaging modalities have limitations on the field-of-view (FOV) that they can image at a particular resolution. For example, a previous multi-scale imaging approach, used for studying fluid catalytic cracking particles (with  $\sim 100 \mu\text{m}$  diameter), employed FIB-SEM that could image volumes of  $2 \times 2 \times 2 \mu\text{m}$  at a resolution of  $20 \times 20 \times 20 \text{ nm}$  [5]. However, this voxel resolution is above the size of smaller mesopores and micropores, that can be probed with gas sorption. In addition, a typical catalyst pellet (5 mm diameter, 5 mm long) would contain  $10^{10}$  such image volumes, each of which might be

\* Corresponding author.

E-mail address: [sean.rigby@nottingham.ac.uk](mailto:sean.rigby@nottingham.ac.uk) (S.P. Rigby).

<https://doi.org/10.1016/j.cej.2022.139122>

Received 30 March 2022; Received in revised form 24 August 2022; Accepted 6 September 2022

Available online 12 September 2022

1385-8947/© 2022 The Authors. Published by Elsevier B.V. This is an open access article under the CC BY license (<http://creativecommons.org/licenses/by/4.0/>).

different in internal properties, and have some type and degree of spatial correlation, and thus may not be completely randomly distributed [6]. For imaging data to obtain the typical properties of a porous solid, then the FOV must encompass the representative volume or correlation length of the structure being imaged.

However, for highly heterogeneous materials, some other means to link together characterisation data may still be needed. In this work it will be seen how indirect characterisation methods, that can span many orders of magnitude in pore sizes, like gas overcondensation and mercury porosimetry, can link together the various levels in the imaging hierarchy.

For hierarchical or multi-scale structures requiring imaging with multiple modalities, some sort of upscaling procedure is required to link together data acquired at different length-scales [4,7,8]. A variety of upscaling procedures have been adopted in the literature. One such procedure involves identification of a set of different phases at a larger length-scale, such that regions that are considered as belonging to the same phase have similar properties at smaller length-scale. In rock structures these different phases might be identified with different types of mineral grains, where disparities in the mineralogy (e.g., quartz, illite etc.) leads to different phases with markedly different properties to each other [4]. However, some porous materials, such as industrial materials, are less discretely variegated such that useful identification of a limited set of such phases is impossible [2]. An alternative approach employs pore bond network models with separate bonds to represent microporosity in series or parallel with macroporosity. One such approach used an SEM image-based method to construct a multi-scale pore network model that incorporates multiscale pore structure spatial and statistical properties at different resolutions [7,8]. Other upscaling procedures rely upon random allocation of porosity and transport properties to individual lower length-scale regions in grids representing an upper length-scale [5]. However, many industrial materials have non-random distributions of lower length-scale properties over larger length-scales [6]. In such cases, an alternative strategy is required.

The indirect, mercury, or Wood's metal, intrusion methods have been combined with complementary SEM and/or CXT imaging to provide contrast agents to improve image quality of the latter, and/or to deshield pore size distributions of the former, in order to obtain exhaustive void space characterisations [9–11]. However, an alternative strategy for dealing with highly complex porous media, that has been proposed [6,12,13], is to directly sift the various pore structural features for their importance to mass transport. This is achieved by progressively eliminating particular, chosen ranges of pore sizes from the transport network, via controlled pore-filling with an obstructing phase (e.g., mercury, ice, or water) using a porosimetric technique, and determining the subsequent impact on mass transport rates of a fluid. This approach is interventionist and experimental, and, thus, differs from modelling approaches in the past that have aimed at determining the importance of particular aspects of the pore structure to mass transport by computer simulation on model structures modified in various ways [14–16]. If a modelling approach is to be truly a priori predictive of mass transport, then it requires an exhaustive characterisation of the void space to ensure the structural model contains all the key features of the void space pertinent to mass transport to the requisite detail. The level of accuracy and comprehensiveness needed for the structural model may not be practicable, or even possible, with current computing power, for very complex porous solids. Hence, statistical approaches based upon simplified pore structural models are often used [2,16]. However, it is then not clear how the supposed important feature of the simplified pore network model relates to the more complex, real network, or how to select the key aspects of the void space to incorporate into models.

In previous work using the sifting approach, entrapped mercury was used to obstruct pore structural features in tableted methanol synthesis pellets, made using roll compacted (RC) feed, and compacted to two different densities [6]. It was found that mass transport was dominated by cracks through the pellet, and voids formed via the splintering of the

edges of feed particles during compaction. However, the comprehensiveness of the pore characterisation was limited due to the use of only conventional gas sorption experiments to probe the void space left accessible following mercury entrapment, and the limitations on the resolution of the CXT imaging employed. Characterisation of macroporosity can be problematic, and the issues and potential solutions have been reviewed [17]. In this work, the gas overcondensation method will be used to expand the range of pore sizes that can be probed up to very large macropores. The gas overcondensation method used in this work, therefore, overcomes previous failings [6] with missing the largest macropores within the methanol catalyst pellets using both conventional adsorption, because capillary condensation was not achieved in these macropores, and also mercury porosimetry, because these macropores were shielded by very small necks for which intrusion would have required pressures in excess of the maximum possible for the apparatus used (414 MPa). Gas overcondensation, thus, makes available the full boundary desorption isotherm for use in percolation modelling not possible otherwise. In addition, multi-modal imaging, employing both high and low resolution CXT, together with FIB-SEM, will be used to improve interpretation of each other, as well as of the indirect pore characterisation methods, in addition to providing spatially-resolved information.

It is often suggested that model porous materials, such as MCM-48 or SBA-15, with controlled pore geometry, often achieved via templating or etching procedures, can inform interpretation of indirect pore characterisation methods [2,18]. These types of materials can aid the testing of fundamental theories for limited length-scale phenomena, such as the origins of single pore hysteresis in simple geometries [2,18,19]. However, these materials, necessarily, have limited unit cell sizes, and as will be seen here, the forms of characterisation data for disordered industrial materials are not just composites of that for model materials. Indeed, it will be seen here that characterisation data is dominated by pore-to-pore co-operative effects that are sample-spanning over macroscopic length-scales. Hence, the characterisation process must address the real, disordered material itself even in the first instance.

The main aim of the current work is to particularly identify the key pore structural features that impact mass transport as a result of the particular fabrication route employed, and thereby inform potential future strategies for improved manufacturing of the tablets. It will be seen that, for the particular pellets studied here, these key features involve the macroscopic spatial distribution of the mesoporosity. In this work methanol synthesis pellets made using two very different types of feed, produced by spray-drying or roll-compaction, will be studied. This is to examine how these different fabrication methods affect the finished pellet properties. Both the starting feed particles and the finished tablets will be studied. It will be seen how gas overcondensation can probe very small void spaces not accessible to mercury porosimetry and many imaging modalities, as well as probing very large macropores with the same technique. Multi-scale imaging, including lower resolution CXT (down to a few microns), higher resolution CXT (down to hundreds of nm), and FIB-SEM (down to a few nm), will be used to improve interpretation of the indirect methods and each other. It will be seen how this new combination of methods can be used to determine the key features of the void space that control gas-phase uptake into the porous pellets, and identify their relationship to the fabrication process and raw materials.

## 2. Theory

Mass transport properties can be characterised by kinetic gas uptake experiments. Kinetic mass uptake data, comprising amount adsorbed versus time, typically takes the mathematical form of an exponential growth, and, thus, is often fitted to the so-called Linear Driving Force (LDF) model [2]. The characteristic parameter of this process is the mass transfer coefficient, denoted  $k$ . The LDF  $k$ -value is defined by the function [2]:

$$M = M_0(1 - e^{-kt}) \quad (1)$$

where  $M$  the amount of nitrogen adsorbed at time  $t$ ,  $M_0$  is the ultimate total adsorbed amount of nitrogen for the adsorption pressure point, and  $k$  is the mass transfer coefficient. The apparent mass transfer coefficient, obtained from a fit to raw uptake data, must be corrected for the effect of concurrent adsorption using the slope of the isotherm at the relevant adsorption pressure point. In this way the actual mass transfer coefficient is obtained.

For a porous sample, the mass transfer coefficient  $k$  depends upon the intrinsic effective diffusivity of the porous material, composed of the reference diffusivity  $D_A$ , the porosity (voidage fraction) and tortuosity of the medium, plus the diffusion penetration depth  $a$ , and a geometric factor, which is 15 for a spherical particle [2]:

$$k = \frac{15D_A \varepsilon}{a^2} \quad (2)$$

The reference diffusivity will be the bulk molecular diffusivity in the molecular diffusion regime, and the Knudsen diffusivity for the critical pore size in the Knudsen regime. If a fraction of a porous network is removed in some manner, but the reference diffusivity and the particle overall size and geometry remain constant, then the ratio of the original tortuosity  $\tau_0$  to the subsequent tortuosity  $\tau$  will be given by:

$$\frac{\tau_0}{\tau} = \frac{k}{k_0} = \frac{\varepsilon_0}{\varepsilon} \quad (3)$$

where the subscript 0 denotes the parameter for the original porous network and the lack of subscript represents the general parameter for any modified network.

It has been proposed that, for multi-scale porous solids, the total tortuosity  $\tau$  has contributions from different length-scales, such that the total tortuosity is given by [20]:

$$\tau = \tau_a \tau_e \tau_i \quad (4)$$

where  $\tau_a$  is the macroscopic tortuosity, describing the pore structure over length-scales of the whole pellet (mm),  $\tau_e$  is the mesoscopic contribution to the tortuosity, which describes tortuosity measured over length-scales of a few pore diameters up to scales at which macroscopic heterogeneities become important, and  $\tau_i$  characterises tortuosity over length-scales of up to a few pore diameters. Eq. (4) has been found, via both computer modelling and experimental validation, to successfully relate the particular different tortuosities obtained from magnetic resonance imaging and pulsed-field gradient NMR methods that probed the total and *meso*-/micro-scale tortuosities, respectively [20,21].

The macroscopic structure of the catalyst pellets studied in this work will be modelled by three-dimensional, random pore bond networks. Such networks consist of lattices of pore bond elements that meet at lattice node junctions. The typical number of pore bonds meeting at a node, averaged over the whole lattice, is called the connectivity  $Z$ . The overall size of the lattice measured in lattice bond units is denoted  $L$ . The parameters  $Z$  and  $L$  can be determined from percolation analysis of gas sorption data using a method based upon that developed by Seaton [22]. Percolation analysis is carried out in terms of percolation variables, the values of which are calculated from pore diameter distributions, and the branches of the hysteresis loop in gas sorption isotherms.

The Seaton [22] percolation analysis neglects single pore hysteresis, such that adsorption and desorption in a single lattice bond is considered reversible, and, thence, assumes that all hysteresis arises from network-based pore-blocking effects. This is considered reasonable if the pore units represented by model bonds are extensive, since adsorption in very long pores tends to that for the equilibrium mode, or dead-end pores [2]. Therefore, in the percolation analysis of gas sorption hysteresis, the bond occupation probability at a particular pressure is given by:

$$X = \frac{\text{The number of pores below their critical condensation pressure}}{\text{The total number of pores in the network}} \quad (5)$$

where  $X$  represents the number fraction of pores from which condensate would have evaporated in a perfectly connected network. Assuming that the pores have a cylindrical geometry, the pore number distribution as a function of pore diameter is calculated from the volume-weighted pore diameter distribution obtained from the adsorption isotherm. The number,  $n_i$ , of pores of diameter  $d_i$  is given by:

$$n_i = \frac{V_i}{\pi \frac{d_i^2}{4} l_i} \quad (6)$$

where  $V_i$  is the incremental volume of pores with diameter  $d_i$ , and  $l_i$  is the average pore length for such pores. It is assumed that pore length is always greater than diameter, and thus diameter is the characteristic pore dimension for adsorption. In the original Seaton method [22] it was assumed that the average pore length is the same in each pore size interval. However, here, as in previous work [23], it will be allowed that the average pore length can depend upon diameter, such that:

$$l_i = m \cdot d_i^\alpha \quad (7)$$

where  $m$  and  $\alpha$  are constants. The set of  $X$  values (one for each data point  $i$  on the adsorption isotherm) is then given by:

$$X_i = \frac{\sum_{j=1}^i n_j}{\sum_{j=1}^N n_j} \quad (8)$$

where  $N$  is the total number of pore size intervals.

The accessibility,  $X^A$ , is the number fraction of pores that are both below their critical pressure and have access to the surface, either directly or via a network of vapour-filled pores. Hence, in other words, it is the fraction of pores from which evaporation of condensate has actually occurred. The experimental values of  $X^A$  are calculated from the deviation between the separate pore-blocked desorption isotherm and unshielded adsorption isotherm according to the method described previously by Seaton [22]. The experimentally derived pairs of values of  $X$  and  $X^A$  are then fitted to a universal scaling relation  $G$  such that:

$$L^{\beta/\nu} Z X^A = G[(ZX - 3/2)L^{1/\nu}] \quad (9)$$

where  $\beta$  and  $\nu$  are critical exponents which take values of 0.41 and 0.88, respectively. The generalised scaling relation  $G$  was constructed using the simulation data of Kirkpatrick [24] for cubic lattices.

Mercury porosimetry is only a relative measure of pore size unless properly calibrated values of contact angle  $\theta$  and surface tension  $\gamma$  are used. By using electron microscopy data for controlled pore glasses as an independent measure of pore sizes, Kloubek [25] obtained expressions of the form:

$$\gamma \cos \theta = A + \frac{B}{r} \quad (10)$$

where  $A$  and  $B$  are constants whose values are dependent on whether the mercury meniscus is advancing or retreating, for these parameters. The values of these constants found for the controlled pore glasses, and their pore size ranges of application, are given in Table 1.

**Table 1**  
Values of Kloubek [25] parameters for use in Equation (10).

	A	B	Range of validity (nm)
Intrusion	−302.533	−0.739	6–99.75
Retraction	−68.366	−235.561	4–68.5

### 3. Materials and methods

#### 3.1. Samples studied

Fresh methanol synthesis catalyst pellets made using either spray dried (SD) or roll compacted (RC) feed materials were studied in this work. The Cu:Zn:Al molar ratio was 4.4:1.6:1 for both materials. The initial materials preparation used standard precipitation techniques employing metal nitrate precursor salts. The catalyst pellets were formed by a bi-directional axial compaction process. The SD and RC pellets are mesoporous cylindrical tablets with average dimensions of  $\sim 5.5 \times 3.5$  mm (base diameter  $\times$  height). The SD pellets had an average BET surface area of  $96.2 \text{ m}^2\text{g}^{-1}$ , and the RC pellets an average BET surface area of  $88.1 \text{ m}^2\text{g}^{-1}$ . Tables 2 and 3 contain further details and properties of the samples studied. The pellets were characterised by gas sorption both in their whole pellet and fragmented ( $\sim 53\text{--}73 \mu\text{m}$  powder particle size) forms.

It is noted that the sample mean pore volumes obtained from gas overcondensation exceed those from mercury porosimetry. This is because the samples contain macropores that are shielded by narrow necks too small to intrude with the maximum pressure possible with the mercury porosimeter used.

#### 3.2. Integrated mercury porosimetry and gas sorption

The integrated mercury porosimetry and gas sorption technique consists of a series of experiments conducted on the same sample. Fig. 1 shows the schematic representation of the gas-mercury-gas procedure used during the experiments. The nitrogen sorption isotherms were measured at liquid nitrogen temperature (77 K) using a Micromeritics 3Flex physisorption analyser. Approximately 0.8 g of the sample (4 cylindrical pellets) was weighed and placed into a pre-weighed standard physisorption sample tube with a sealing frit placed at the top to prevent the sample from being evacuated into the 3Flex manifold. The tube (with sample) was then loaded into the degassing station and initially degassed at room temperature until a vacuum of 0.02 mmHg was reached. The sample temperature was then raised to  $140^\circ\text{C}$  by using a heating mantle, and the sample was left under vacuum for 24 h. The thermal pre-treatment drives off any physisorbed water on the sample but does not change the sample morphology. After the 24 h had passed, the heating mantle was removed, and the sample was allowed to cool down to room temperature. The sample tube and its contents were then re-weighed to obtain the dry weight of the sample. Isothermal jackets were then placed around the sample tubes before reattaching them to the analysis port to begin the automated gas sorption analysis. The isothermal jacket ensures a constant thermal profile of 77 K along the length of the sample tube during the analysis stage. Nitrogen purity was 99.995 %. The isotherms consisted of approximately 60 adsorption and 50 desorption points. Gas sorption was measured over the relative pressure ( $P/P_0$ ) range of 0.01 to 0.995 for adsorption isotherm and 0.995 to 0.10 for desorption isotherm. The saturation pressure ( $P_0$ ) was measured for each data point on the isotherm.

Once the first nitrogen gas sorption experiment was finished, the samples were allowed to reach room temperature ( $\sim 295.15 \text{ K}$ ) and then quickly transferred to a mercury intrusion porosimetry (MIP) machine to

**Table 2**

Characteristics of the whole pellet samples. Porosity values were obtained from mercury porosimetry. The bulk density was obtained from helium pycnometry.

Sample	Porosity (%)	Bulk density ( $\text{g}/\text{cm}^3$ )	BET ( $\text{m}^2/\text{g}$ )	Cylinder dimension (diameter $\times$ height)
Fresh SD	47.1 %	2.2	$96.16 \pm 2.56$	$5.5 \times 3.4 \text{ mm}$
Fresh RC	48.1 %	2.3	$88.13 \pm 10.70$	$5.6 \times 3.5 \text{ mm}$

**Table 3**

Sample mean ( $\pm 1$  std. error) specific pore volumes and modal pore diameters of the samples determined by two different methods.

Sample	Hg pore volume ( $\text{ml}/\text{g}$ )	$\text{N}_2$ sorption pore volume ( $\text{ml}/\text{g}$ )	Hg modal pore diameter (nm)	$\text{N}_2$ modal pore diameter (nm)
Fresh SD	$0.224 \pm 0.006$	$0.231 \pm 0.003$	9.4	9.3
Fresh RC	$0.217 \pm 0.012$	$0.226 \pm 0.002$	10.9	10.4

entrap mercury into the pores. Mercury intrusion and retraction curves were measured using a Micromeritics Autopore IV 9500, which can generate a maximum pressure of 414 MPa (60,000 psia). Mercury intrusion data was generated for the range specified in the scanning curve pressure points followed by retraction back down to atmospheric pressure. The sample was transferred into a penetrometer, and the weight of the penetrometer and sample was recorded. The penetrometer (with sample) is then placed in the low-pressure port of the instrument. During the low-pressure analysis, the sample is evacuated up to 50  $\mu\text{mHg}$  to drive off any water vapour or atmospheric gases in the pore network. The sample bowl is then filled with mercury while the entire system is still under low pressure. Data collection begins at a pressure of 0.5 psia, which is enough to cause mercury to penetrate sample pores larger than  $360 \mu\text{m}$  in diameter. After the low-pressure analysis was completed, the assembly weight (penetrometer + sample + mercury) was recorded, the penetrometer was transferred to the high-pressure port, and the chamber was closed tightly. The penetrometer is placed vertically in the high-pressure port, and it is surrounded by oil, which is the hydraulic fluid the instrument uses to generate high pressures. As the hydraulic fluid pressure rises, it is transmitted to the mercury in the penetrometer via its open capillary stem. An equilibration time of 15 s was used for each data point.

Once the mercury intrusion experiment was finished, the sample was immediately discharged from the penetrometer, recovered, and returned to the 3Flex sample tube, where the rate of adsorption and the conventional adsorption experiments were repeated. The sample was first cooled to 77 K by manually raising the Dewar flask, allowing the sample to freeze for approximately 30 min. This part was crucial in the post mercury entrapment steps since it freezes the mercury in-place to ensure that it all remains immobilised within the pellets. The integrated rate of adsorption-mercury porosimetry aims to selectively block specific pore sizes and then study how important those pores were to the rate of mass transport before and after their removal. Previous experiments where the mercury was thawed and re-frozen after a week prior to subsequent gas sorption have shown that the mercury ganglia did not move around over this timescale or due to the freezing since the shapes of the gas sorption isotherms remained the same [6].

#### 3.3. Rate of adsorption (ROA) procedure

The rate of adsorption technique works by dosing a known quantity of nitrogen gas onto the sample and then recording the amount of gas adsorbed and the corresponding pressures over time. The dosing quantity was taken from the BET monolayer capacity ( $V_m$ ). An additional 5 cc of gas was added to this amount to compensate for the initial expansion of the gas into the free space of the sample tube. This is because the gas first fills the sample tube before adsorbing onto the sample surface. The number of readings of pressure was set at 1000 readings per dose. The ROA data was collected at the lowest pressure point in the isotherm. In this region of the isotherm, there is negligible obstruction from adsorbed phase, and the diffusion is in the Knudsen regime and corresponds to the process conditions in the reactors in which the methanol synthesis pellets are used. The rate of uptake data was collected both before and after mercury entrapment.



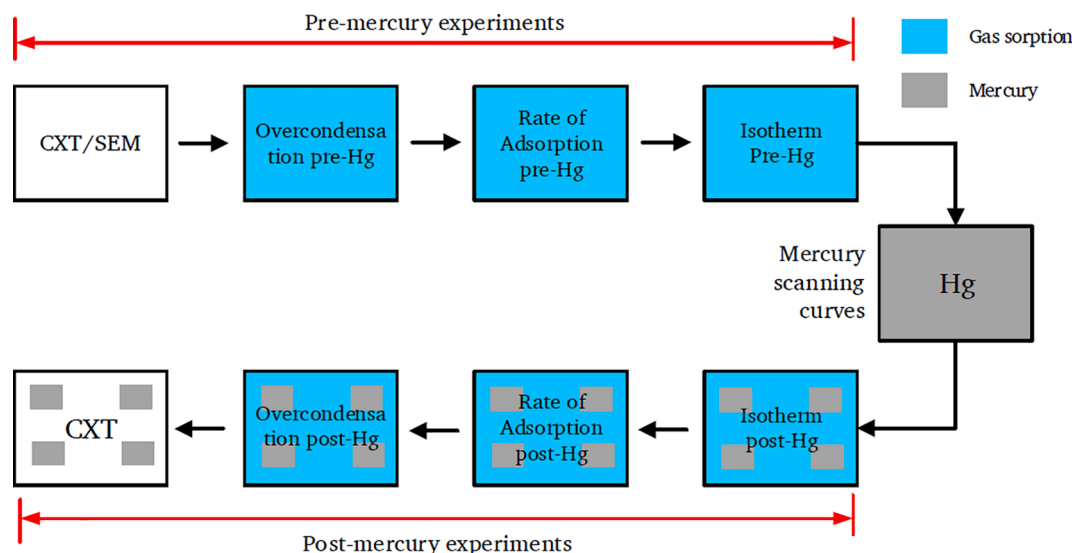


Fig. 1. A schematic representation of the integrated mercury porosimetry-gas adsorption-imaging technique.

### 3.4. Overcondensation gas sorption procedure

The nitrogen overcondensation (OC) experiment was carried out on a Micromeritics ASAP 2020 physisorption analyser. The OC experiment is explained in more detail in previous work [26] and uses a method similar to that described by Murray et al. [27]. The OC experiment involves “flooding” the sample chamber with condensed liquid nitrogen to submerge the sample in liquid nitrogen to investigate any porosity beyond the instrument upper limit for the conventional isotherm ( $P/P_0 > 0.995$ ). The conventional isotherms for these materials clearly show that porosity exists beyond the conventional instrument’s upper limit. Once the sample is fully submerged in liquid nitrogen and total pore filling is achieved, the pressure in the tube is lowered to just below the saturated vapour pressure of nitrogen such that the bulk condensate vapourised completely while all the sample internal porosity is liquid-filled. Once this step has been achieved, the first data point on the overcondensation desorption isotherm can be measured. This point corresponds to the total pore volume of the sample. The pressure is then progressively lowered in small steps, and the rest of the desorption isotherm was obtained in the usual way. The reported raw data (relative pressure and volume adsorbed (cc/g STP)) is greatly offset to what would be expected due to the very large amount of gas (from the bulk liquid nitrogen) that must be removed before the onset of desorption from the sample porosity. The data were normalised to a quantity of gas on the adsorption isotherm below a relative pressure of 0.42 where, for the conventional isotherm, the desorption data coincides with the adsorption data. The OC data was collected for the samples both before and after mercury intrusion.

### 3.5. Computerised X-ray tomography and dual-beam electron microscopy

#### 3.5.1. Low resolution computerised X-ray tomography (CXT)

For the low-resolution CXT scans, the pellets were imaged before and after mercury entrapment using a Zeiss Xradia Versa XRM-500 to acquire 3D image stacks. The X-ray source for the Xradia 500 Versa instrument was set to 140 kV and power of 10 W. The apparatus’s macro lens (0.4X) was used to image the whole pellets with a diameter of 5.4 mm with 360 degrees rotations. The average pixel size for empty pellets was 5.6  $\mu\text{m}$ , and the average pixel size for samples with mercury was 5.9  $\mu\text{m}$ . Image acquisitions parameters were the same for all the empty samples and the samples with entrapped mercury. The scan times were roughly 2 h for the empty samples and 2.5 h for mercury-filled pellets. Both samples were scanned with 1600 projections per 360 degrees scan.

Each 3D image stack contained 1016 slices with dimensions of 1024  $\times$  1024 pixels and 24-bit depth.

#### 3.5.2. High resolution computerised X-ray tomography (CXT)

Multi-scale imaging of the feed materials was performed by X-ray tomography at the TOMCAT beamline (Swiss Light Source). The high-resolution microscope (Optique Peter), with 4 $\times$ , 10  $\times$  and 20  $\times$  magnification and LuAG:Ce 20  $\mu\text{m}$  scintillator, was used in combination with a Pco.Edge 5.5 detector, yielding an effective pixel size of 1.63, 0.65 and 0.325  $\mu\text{m}$ , respectively. Spray-dried (SD) feed material was scanned with the energy of 20 keV and 150 ms exposure time per projection. Monochromatic energy of 30 keV and exposure time of 500 ms was used to acquire images of bigger roll compacted (RC) particles. Both samples were scanned with 2500 projections per 180 degrees scan. The 3D volume data sets were reconstructed using the propagation-based phase-contrast method [28] and the gridrec algorithm [29].

#### 3.5.3. Focussed ion beam- scanning electron microscopy (FIB-SEM)

The serial milling images were acquired using a Crossbeam 550 (Carl 206 Zeiss Microscopy) instrument equipped with a cryo-stage and integrated VCT500 vacuum transfer system for FIB-SEM imaging. The samples were mounted onto a pre-tilted sample holder, and each was transferred into the Crossbeam 550 using the VCT500 shuttle. Once the samples were inside the instrument, an automated FIB milling algorithm was subsequently set up and executed. To ensure that the unsupervised automated FIB milling was successful, the equipment was properly aligned and calibrated on a weekly basis. The Crossbeam 550 was also calibrated to mill a cross-section with dimensions of 10  $\times$  30  $\times$  10  $\mu\text{m}$  (XYZ) through the sample to acquire a 3D image stack. A fixed voltage of 30 kV and a current of 700 pA was used to generate the FIB images.

## 4. Results

### 4.1. Imaging of empty spray-dried (SD) feed pellets

#### 4.1.1. Lower resolution CXT

Fig. 2 shows typical examples of reconstructed 2D radial cross-section slice CXT images of the SD feed pellets. In Fig. 2, the individual SD feed particles making up the pellet can be seen by virtue of a distribution in density in the particles evident from the variation in average pixel intensity in each SD feed particle. There are also many smaller, dark black spots, which correspond to the graphite lubricant particles. In addition, in Appendix Figure A2 in the Supplementary Data,

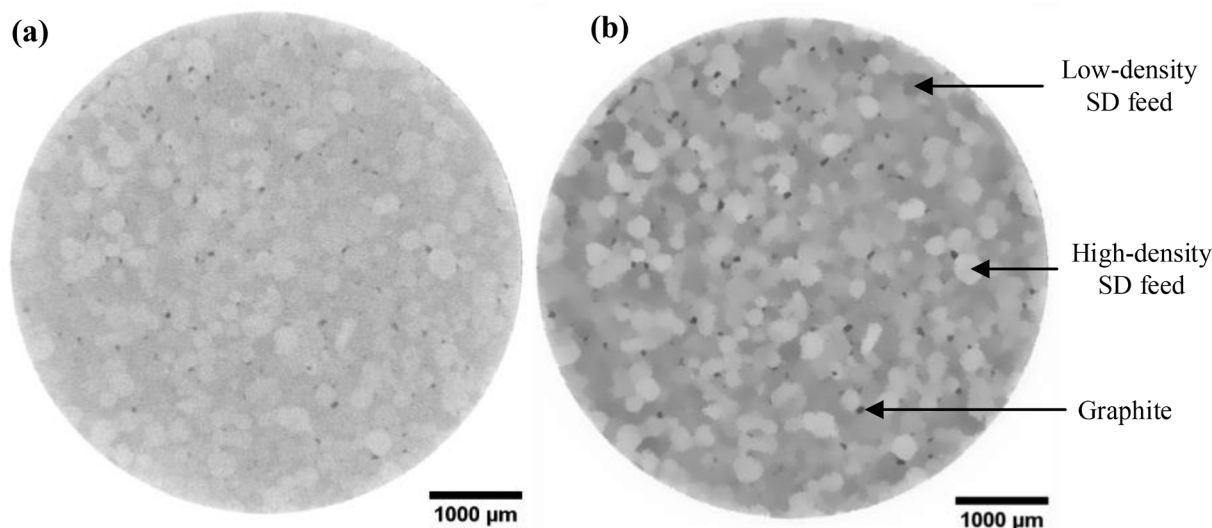


Fig. 2. (a) Raw 2D radial slice before filtering, and (b) after applying contrast and histogram equalisation and non-local means filters.

we have included an intensity profile for a typical cross-section of a SD feed pellet. Since the pixel resolution is generally larger than the length-scale of variations in solid matrix density (except for carbon particles), the variations in the density profile are dominated by pellet voidage effects.

Fig. 3 shows the 3D reconstruction and segmentation of the stack of the 2D slices for the SD feed pellet. The image has been segmented into three bins of intensity corresponding to the very low-density carbon particles, low density SD feed particles and high-density SD feed particles. From the segmentation of the three separate phases shown in Fig. 3, it can be seen that their distributions are pervasive throughout the pellet and there are no signs of segregation by density.

#### 4.1.2. High resolution CXT

Fig. 4 shows a 3D reconstruction and 2D radial cross-section slice

CXT images of the SD feed particles used to make the SD feed pellet. To aid the discernment of the relationship between the pellet and feed particles, a lower resolution 2D radial cross-section slice CXT image of the pellet has also been included. From Fig. 4, it can be seen that the spherical SD feed particles that make up the pellet are themselves composite structures. The SD feed particles are themselves made up of a range of different types of smaller-scale ( $\sim 1\text{--}10\text{ s } \mu\text{m}$ ) particles. Some smaller particles are solids of very high density, as shown by the bright white pixel intensity. Other particles consist of bright white shells surrounding large voids (denoted ‘bubble pores’). There are also lower density particles. In between the smaller particles are some void spaces. The variation in the density of each individual SD feed particle in the lower resolution CXT image may be associated with variation in numbers of the high density solid smaller particles, and the shells, evident in the cross-sections of different smaller particles.

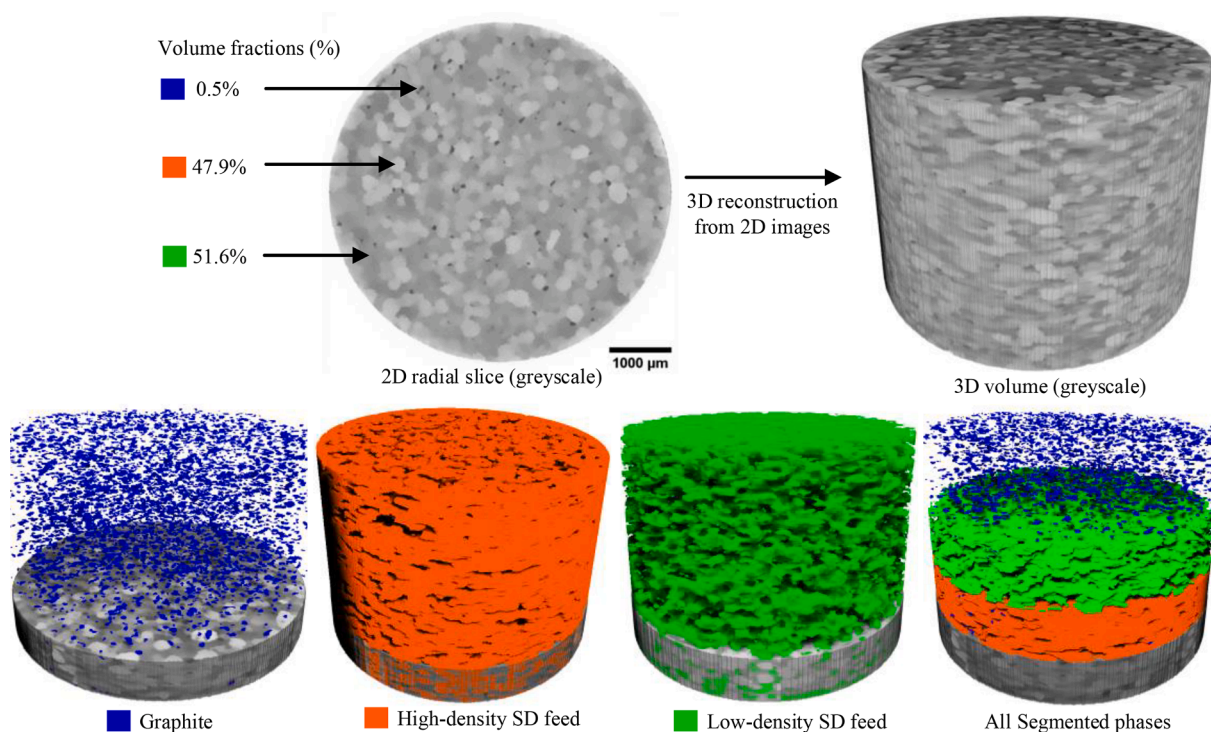
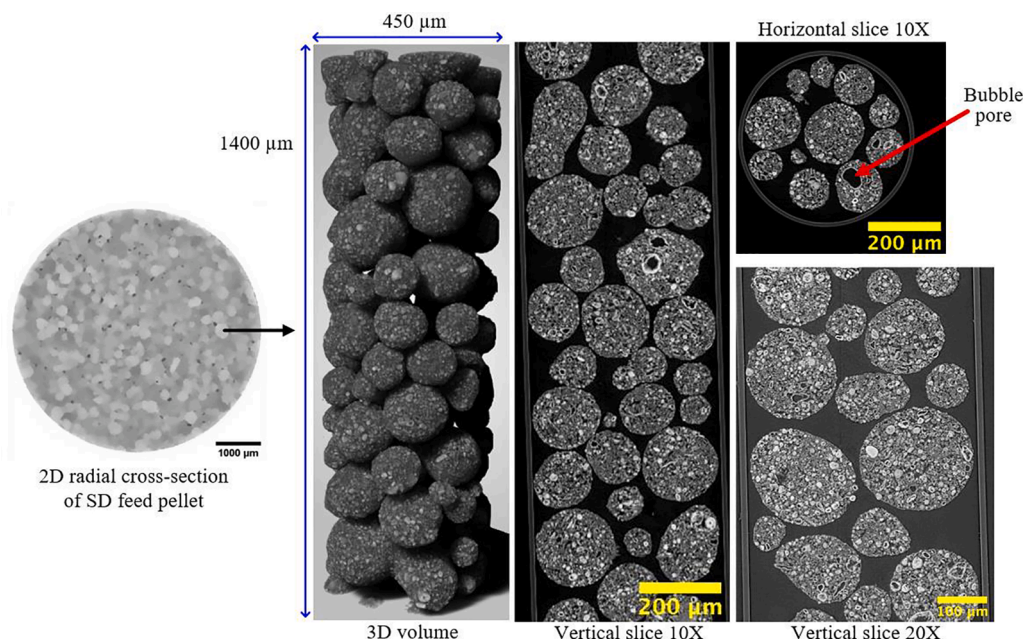


Fig. 3. 3D reconstruction and segmentation of the stack of the 2D slices for the empty SD feed pellet.



**Fig. 4.** 2D radial cross-sections and 3D reconstruction of high resolution CXT image of SD feed particle used to make the SD feed pellet. Also shown on the left side of the figure, for comparison purposes, is a low resolution image of a whole SD feed pellet with an arrow indicating a corresponding individual constituent feed particle.

#### 4.1.3. FIB-SEM imaging

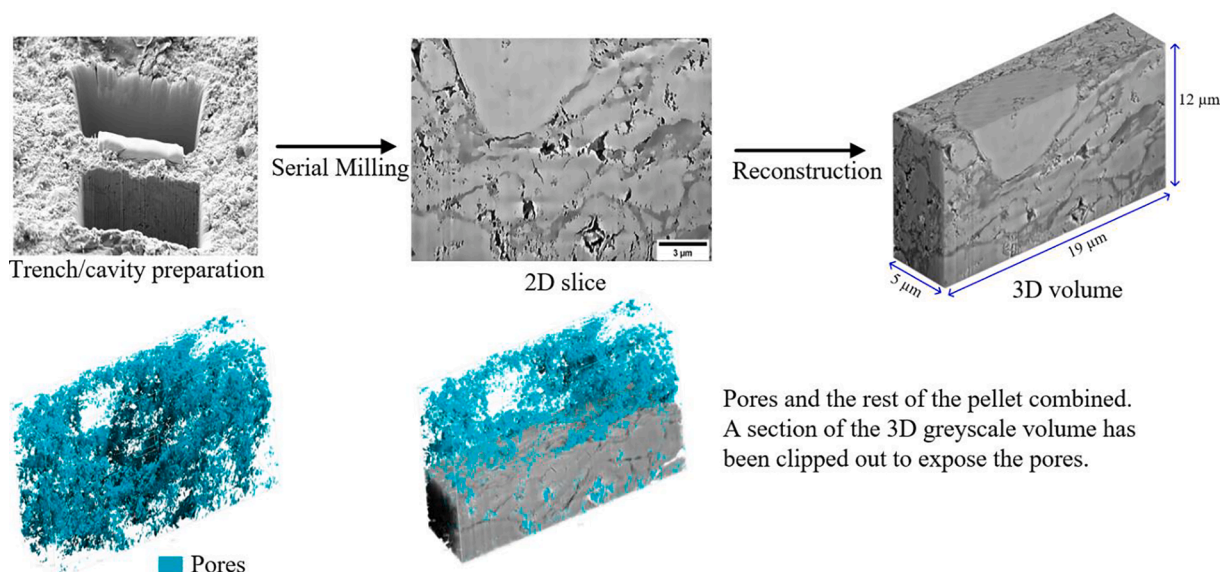
Fig. 5 shows an example of a FIB-SEM trench site, 2D slice SEM image and a 3D volume reconstruction from 510 slices. Also shown in Fig. 5 is the results of segmentation of the reconstructed image into solid phase and porosity.

Table 4 shows values of porosity obtained from segmentation of image reconstructions of two FIB-SEM sample trenches from each of two samples of RC and SD feed pellets. It is noted that the field-of-view of the 3D volume reconstruction exceeds the correlation length of the visible underlying structure, since the voidage fractions reach a constant value measured over length-scales below that of the sampled volume. However, it can be seen that there is some variation in the macroporosity values detected in each trench of the SD feed pellet, which may reflect the spatial variation in density and porosity over much larger length-

**Table 4**

Voidage fractions (porosity) of pores identified via image analysis of 3D reconstruction images from two samples of FIB-SEM trenches within fresh spray dried (SD) and roll compacted (RC) feed pellets.

Sample	Porosity (Sample 1)/%	Porosity (Sample 2)/%
Fresh SD	2.4	3.7
Fresh RC	2.1	3.2



**Fig. 5.** 2D and 3D reconstructed grayscale FIB-SEM images and segmentation result for fresh spray dried pellet. Also shown on the figure is the trench/cavity site. The scale bar corresponds to 3 µm.



scales as seen in the CXT images, since the locations in pellets for FIB-SEM trenches were randomly chosen.

## 4.2. Imaging of empty roll-compacted (RC) feed pellets

### 4.2.1. Lower resolution CXT

Fig. 6 shows typical examples of reconstructed 2D radial cross-section slice CXT images of the RC feed pellets. In Fig. 6, it can be seen that there are many irregularly-shaped regions of varying size and density, as inferred from the pixel intensities. There is also some hint of density variation within the irregular shaped regions. The high-density regions are surrounded by darker lower density boundaries. In addition, in Appendix Figure A3 in the Supplementary Data, we have included an intensity profile for a typical cross-section of a RC feed pellet. The solid matrix is generally homogeneous (with the obvious exception of lubricant carbon particles) over the length-scales of the resolution in the CXT images in both Figs. 2 and 6, and thus variations in density are most probably the result of variations in porosity within a given voxel.

### 4.2.2. High resolution CXT

Fig. 7 shows a 3D reconstruction and 2D radial cross-section slice CXT images of the RC feed particles used to make the RC feed pellet. The 2D slice images contain regions of brighter intensity associated with higher density, and darker regions associated with lower density. To aid the discernment of the relationship between the pellet and feed particles, a lower resolution 2D radial cross-section slice CXT image of the pellet has also been included. From Fig. 7 it can be seen that the irregular form of the RC feed particles matches that of the irregular regions seen in the low-resolution image, and thus the latter can be identified as the former. It can also be seen that, to the eye, the close-up views of the individual RC feed particle provided by the high resolution CXT look very similar to that of the lower resolution image of the whole RC feed pellet. Both the whole pellet and the individual feed particles have within them irregular regions of varying density. Hence, the RC feed pellet has the visual appearance of a fractal object, where increasing magnification, provided by the higher resolution CXT, reveals similar structures.

### 4.2.3. FIB-SEM imaging

Fig. 8 shows an example of a FIB-SEM trench site, 2D slice SEM image, and a 3D volume reconstruction from 510 slices. Also shown in Fig. 8 is the results of segmentation of the reconstructed image into solid phase and macroporosity.

Table 4 shows the corresponding voidage fraction values for the macroporosity, detectable over the length-scales probed by the SEM, in each of two reconstructed 3D images for two FIB-SEM trenches from different pellets of the RC feed batch. As with the SD feed particles, the data in Table 4 indicates some variation in local macroporosity values for the RC pellets. From Fig. 8 it can be seen, in the volume sampled, that the texture of the RC feed pellet over length-scales  $\sim 1\text{--}10\text{ }\mu\text{m}$  is very different to that of the SD feed pellet region seen in Fig. 5.

## 4.3. Mercury porosimetry

### 4.3.1. Intrusion and extrusion data

Fig. 9 shows the mercury porosimetry data for the SD and RC feed particles following analysis with the Kloupek [25] correlations. It can be seen that both data-sets show an intrusion step at  $\sim 100\text{ }\mu\text{m}$  that corresponds roughly to the order of magnitude of the size of the individual feed particles, and thus corresponds to intrusion in gaps between them. While the intrusion curves for both types of feed particle have steps of similar volume at  $\sim 10\text{ nm}$ , the SD feed particle intrusion curve has an additional step at  $\sim 1\text{ }\mu\text{m}$ . From a consideration of the high resolution CXT data given in Fig. 4 and Fig. 7, it is likely that this additional step corresponds to intrusion into the bubble pores in the SD feed particle, which are not present in RC feed particles. The pore size at the additional step probably corresponds to pore sizes in the intact shells, or cracks in the shells, around the bubble pores in the SD feed.

Fig. 10(a) and (b) show mercury porosimetry scanning curve data for whole pellets made with SD and RC feed. It can be seen that as the ultimate mercury pressure is increased, then, progressively, more intrusion occurs into ever smaller pore necks. From the mercury extrusion data, it can be seen that, typically,  $\sim 75\text{--}100\%$  of the intruded mercury becomes entrapped, depending upon the ultimate intrusion pressure, with fractionally less mercury becoming entrapped for higher ultimate intrusion pressures.

### 4.3.2. Low resolution CXT imaging of pellets following mercury entrapment

Fig. 11(a) and Fig. 12(a) show typical reconstructed 2D radial slice CXT images of whole pellets following mercury intrusion to a range of pressures. Since mercury is a very electron dense element, the regions of the pellet containing entrapped mercury show up as bright white pixels, while the empty pellet matrix is in shades of grey. From a comparison of the images in Fig. 11(a) and Fig. 12(a), it can be seen that the spatial patterns of mercury intrusion for the two types of pellets are very different. The series of images for the SD feed pellet show mercury intrusion occurs as a defined front that progressively migrates towards

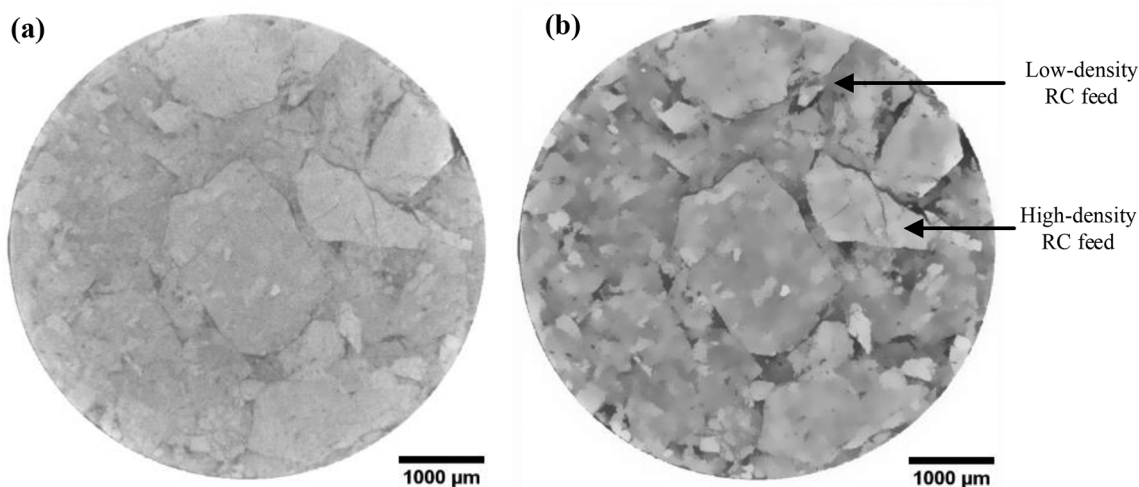
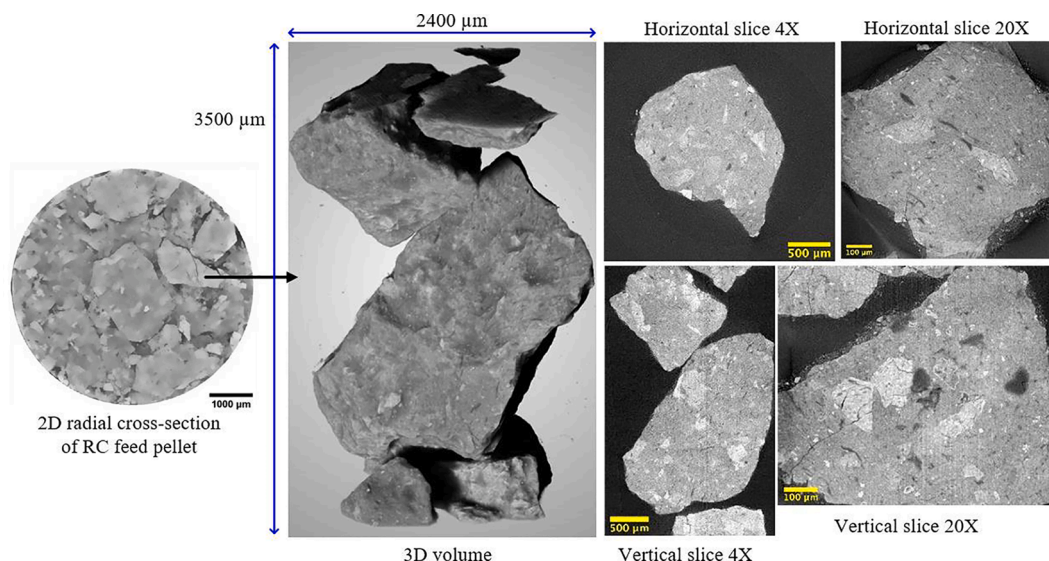
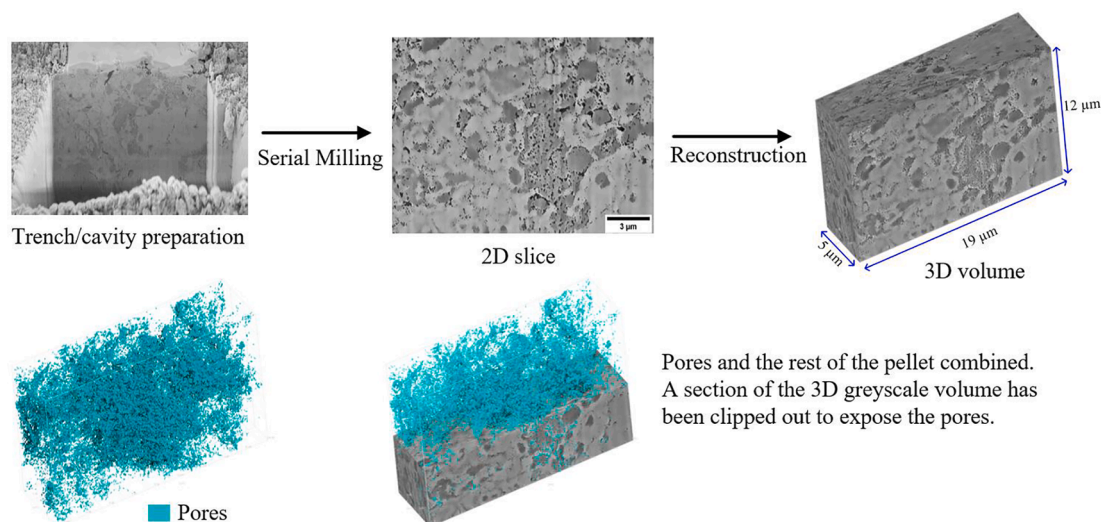


Fig. 6. Typical examples of reconstructed 2D radial cross-section slice CXT images of the RC feed pellets. (a) Raw 2D radial slice before filtering, and (b) after applying contrast and histogram equalisation and non-local means filters. The scale bar corresponds to  $1000\text{ }\mu\text{m}$ .





**Fig. 7.** Lower resolution CXT 2D radial cross-section of whole pellet and showing schematically how it relates to higher resolution 3D reconstruction and 2D radial cross-section slice CXT images of the RC feed particles used to make the RC feed pellet.



**Fig. 8.** Fresh RC FIB-SEM trench site, and 2D and 3D reconstructed grayscale FIB-SEM images and segmentation result for fresh roll compacted pellet. The scale bar corresponds to 3 μm.

the centre of the pellet with increasing pressure. There is thus a 'shrinking core' effect for the remainder of the pellet unintruded with mercury. However, it is noted that behind the front, intrusion of all the void space is not complete, as some SD feed particles remain partly or fully without mercury even once the main intrusion front has moved past. Even once this front has reached the centre of the pellet, following intrusion to a pressure of 14,700 psia, unintruded SD feed particles are clearly evident, as dark circles, in the image.

In contrast, as seen in Fig. 12(a), for mercury intrusion of the RC feed pellet, once mercury has penetrated a band in the outer regions of the pellet at low pressure, further intrusion is more dendritic in form, with percolation achieved by 10,800 psia. The fractal dendritic form of the mercury intrusion path is more clearly evident in the 3D reconstruction CXT images of a partially-intruded RC feed pellet shown in Fig. 12(b). The image has been segmented to distinguish the regions with intruded mercury from the remaining pellet matrix. However, large zones of the pellet are left unintruded. The irregular polygonal form of the dark unintruded zones suggests that they are likely associated with particular RC feed particles within the pellet. Intrusion occurs via cracks, lower

density RC feed particles, and the low-density regions surrounding high density feed particles. Eventually, at the very highest pressures, all of the regions of the pellet are intruded.

Fig. 11(b) shows the segmentation results of the fresh SD pellet following mercury porosimetry up to 10800 psia leading to entrapment filling 15 % of the pore space. The figure depicts 3D renderings of the pellet showing entrapped mercury and the remaining empty pore spaces. The bright white pixels are associated with entrapped mercury as they represent largest X-ray absorbance, whereas the relatively grey regions represent empty void spaces without mercury. The volume fraction based on pixel intensity of mercury (orange colour) from the CXT images is 36.2 %. The rest of the unfilled pore spaces in the pellet represented 63.8 % of the volume fraction.

Fig. 12(b) shows the segmentation results of the fresh RC pellet following mercury porosimetry up to 8600 psia leading to entrapment filling 11 % of the pore space. The mercury entrapment shows a similar pattern as the fresh spray dried pellet as it forms a shrinking core effect. The volume fractions of mercury and empty pore spaces are 33.2 % and 66.8 %, respectively.

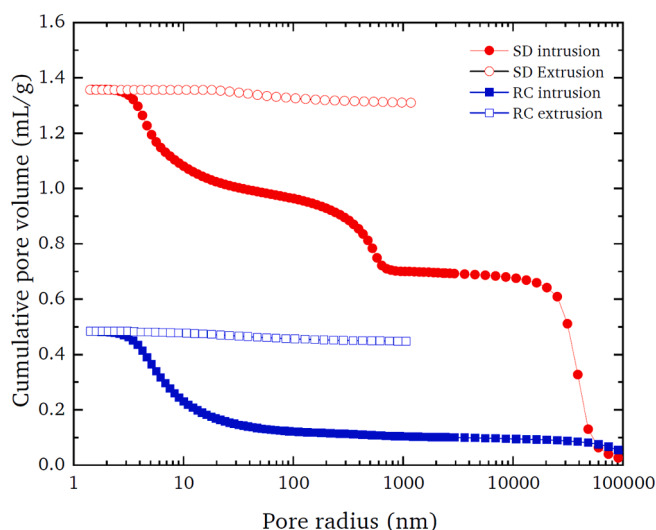


Fig. 9. Mercury intrusion (solid symbols) and extrusion (hollow symbols) porosimetry data for the SD (circles) and RC (squares) feed particles analysed using the Klouček [25] correlations.

#### 4.4. Gas sorption

##### 4.4.1. Isotherms

As mentioned above, the overcondensation technique permits the obtaining of the full boundary desorption isotherm not possible with conventional adsorption. Fig. 13 shows the conventional gas sorption data, and also nitrogen overcondensation boundary desorption isotherms, for empty SD and RC feed pellets, and also for these two types of pellets following mercury entrapment after intrusion to a range of different pressures. From Fig. 13(a) and (c-d), it can be seen that entrapment of mercury following intrusion to 10,800 and 14,700 psia has made the hysteresis loops wider for both the SD and RC feed pellets. This increase in hysteresis width has been made clearer for the RC feed pellet data by raising the isotherms obtained after mercury entrapment by 5.5 and 3.3 cc(STP)/g, as seen in the insets in Fig. 13(c) and (d), since entrapment also led to a more marked decrease in adsorption at lower relative pressures than for the SD feed pellet. In addition, percolation analysis [2,22] has been performed using the overcondensation desorption isotherm and the conventional adsorption isotherm for both the empty samples and those containing entrapped mercury. The analysis was repeatedly conducted assuming different values of the parameter  $\alpha$  in Eq. (7) of 0, -1, or -2 each time (see Appendix Table A1 in Supplementary Data). It was found that the best fit of the experimental data, for both SD and RC feed pellets, to the universal scaling relation (Eq. (9)) was obtained when the parameter  $\alpha$  had a value of -1, suggesting pore bond lengths were inversely proportional to pore diameter. This suggests that, in the real material, the size of domains of similar pore diameter increases with decreasing diameter. The corresponding results for the network model lattice parameters are shown in Table 5. From Table 5, it can be seen, for both types of pellets, that the connectivity declines and the apparent lattice size increases, with increasing mercury entrapment as arises at higher intrusion pressures.

While the overall forms of the hysteresis loops for the conventional nitrogen sorption data for both types of pellet are relatively similar, in contrast, the overcondensation boundary desorption curves reveal some key differences. First, while the Gurvitch volumes for both types of pellet are higher for the overcondensation data, the pore volume missing from the conventional isotherm is larger for the SD feed pellets than for the RC feed pellets. Second, while the overcondensation boundary desorption isotherms show a much sharper percolation knee near the top of the hysteresis loop, not present in the conventional desorption isotherms, the overcondensation data for the empty SD feed pellet also shows a

second, more rounded, percolation knee at relative pressures of  $\sim 0.7$ – $0.8$ , not evident in the overcondensation data for empty RC feed pellets, which have a much straighter, flatter desorption isotherm in this relative pressure region.

From Fig. 13(a), it is noted that the sharp percolation knee near the top of the overcondensation isotherm for the fresh SD feed pellet, first, remains sharp, but is shifted to lower relative pressure, following mercury entrapment after intrusion to 10,800 psia, but then becomes very rounded following mercury entrapment after intrusion to 14,700 psia. In contrast, the second already more rounded percolation knee at relative pressures  $\sim 0.7$ – $0.8$  remains unchanged until mercury is intruded to  $\sim 21,000$  psia, when it disappears. It is noted that the conventional desorption isotherm for the SD feed pellet is effectively a desorption scanning curve. A scanning curve is defined as an isotherm whereby the progressive change in pressure is halted, and the direction of change reversed, before ultimately reaching one of either hysteresis closure points in the full boundary isotherms, which are the isotherms where complete pore-filling with condensate is achieved at the upper end in terms of amount adsorbed. From Fig. 13(a) it can be seen that, while the conventional desorption isotherm descends slightly, it crosses to the overcondensation boundary isotherm well above the hysteresis closure point and also the second more rounded percolation knee.

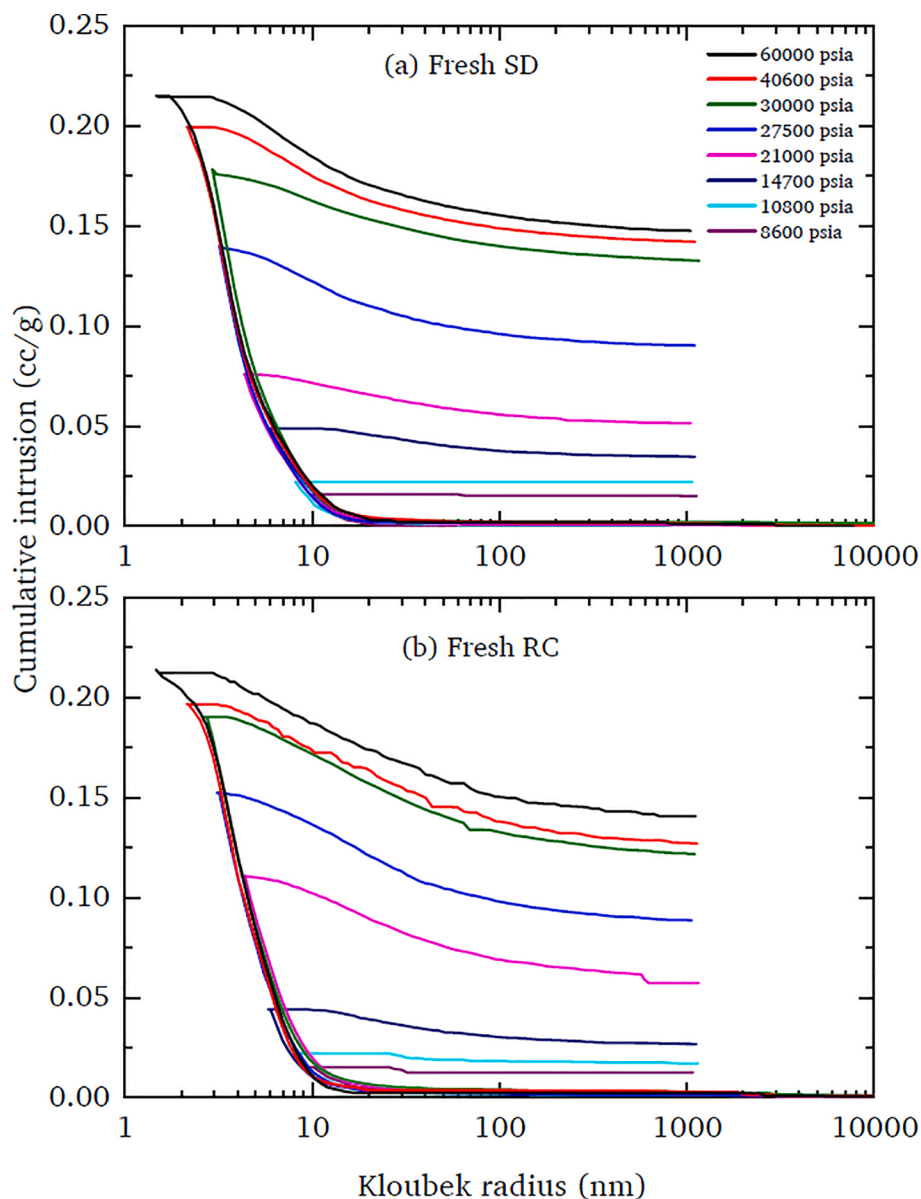
The hysteresis loop was scanned further using a desorption scanning curve with the reversal in the direction of pressure change occurring at a relative pressure 0.85 on the boundary adsorption isotherm. These data are shown in Figure A4 in the Supplementary Material, where it can be seen that the lower pressure scanning curve exhibits different behaviour to the conventional desorption isotherm in that, in contrast, the former is converging on the lower hysteresis closure point.

Fig. 14 compares the conventional nitrogen sorption isotherms for the empty SD feed pellet, with the equivalent data following mercury intrusion to 21,000 and 30,000 psia. From Fig. 14 it is noted that the form of the conventional sorption isotherms following mercury intrusion to 21,000 psia shows a marked kink in the adsorption isotherm at a relative pressure just above 0.8, and a percolation knee at the same amount adsorbed in the desorption branch at a relative pressure of  $\sim 0.7$ . This sharp knee at relative pressure  $\sim 0.7$  is also evident in the overcondensation boundary desorption isotherm in Fig. 13(a). This formation of the kink in the sorption isotherms is what might be expected if there has been a greater loss of larger pores than smaller pores that fill below the kink. The parallel form of the branches of the hysteresis loop in the conventional sorption data following mercury intrusion to 30,000 psia (shown in Fig. 14) may suggest a single pore origin for the hysteresis. The small step down, at a relative pressure of  $\sim 0.4$ – $0.5$ , in the conventional and overcondensation desorption isotherms, that closes the hysteresis, is, based on its position, probably due to cavitation, and suggests some larger pores are shielded by necks smaller than  $\sim 4$  nm.

In order to further probe the impact on gas sorption of macroscopic structural heterogeneities, gas sorption experiments were conducted on powder samples of particle sizes 53–75  $\mu\text{m}$  formed by fragmentation of whole pellets, and these data are given in the Supplementary Material. This particular powder size fraction was chosen as it is similar to that for the original SD feed particles. Fragmented pellet samples were used, instead of original feed particles, as it is possible that the treatment of the pellet following forming of the feed into the tablet, as part of the overall fabrication procedure, may have impacted the mesopore structure, and only the effect of particle size of the final product sample material upon the gas sorption data was required. The data for the powder experiments demonstrate the impact of the bubble pores on conventional adsorption isotherms and the presence of advanced condensation effects.

##### 4.4.2. Pore size distributions

Fig. 15(a) and (b) show the BJH PSDs of the sub-sets of pores that become inaccessible from the exterior, for each stage in the series as the



**Fig. 10.** Mercury porosimetry scanning curve data for whole pellets made with (a) fresh spray dried feed and (b) roll compacted feed material analysed using the Kloube [25] correlations.

ultimate mercury intrusion pressure is increased for progressively higher pressure porosimetry scanning curves for the fresh SD and RC samples, respectively. These difference in PSD plots are obtained by subtracting the PSDs from isotherms for samples following successive mercury scanning curves. In general, a lower pressure scanning curves fills large and medium pores, while a higher-pressure scanning curve fills some of the remaining medium and smaller pores. Hence, access to ever smaller pores declines as the intrusion pressure is increased, as one might expect. It is also noted that the steep decline in incremental volume at the lowest pore size present in each distribution corresponds to the minimum penetrated radius for ultimate mercury intrusion pressures.

Serial nitrogen and water adsorption experiments were conducted on the fresh pellet samples, and details of these experiments and resultant raw data are included in [Supplementary Material Figure A8](#). [Fig. 16\(a\) and \(b\)](#) show the resultant BJH PSDs of the sub-sets of pores that become inaccessible from the exterior, as the pre-adsorbed water partial pressure is increased to progressively higher values for the fresh SD and RC samples, respectively. These differences in nitrogen PSD plots were obtained by subtracting the PSDs from isotherms for samples following

successive water scanning curves. In general, a lower pressure water scanning curves fills smaller pores, while a higher-pressure scanning curve fills the medium and larger pores. Hence, access for nitrogen to ever larger pores decline as the water relative pressure is increased, as one might expect.

#### 4.4.3. Rate of adsorption

The rate of adsorption of nitrogen at very low pressure was measured for empty pellets and for pellets following mercury intrusion to various ultimate pressures. The mass uptake curves obtained were fitted to the linear driving force (LDF) model, and the mass transfer coefficients (MTCs) (denoted  $k$ ) were corrected for adsorption using the slope of the equilibrium isotherm at the point where mass transport was measured [2]. The LDF fitting process is explained further in previous work [6]. The MTCs so- obtained for SD feed and RC feed pellets are shown in [Table 6](#) and [Table 7](#) respectively. As can be seen from [Table 6](#) and [Table 7](#) the MTCs generally decline following mercury entrapment, and the drop increases with increased mercury entrapment, except between 14,700 and 21,000 psia for the RC feed pellets.



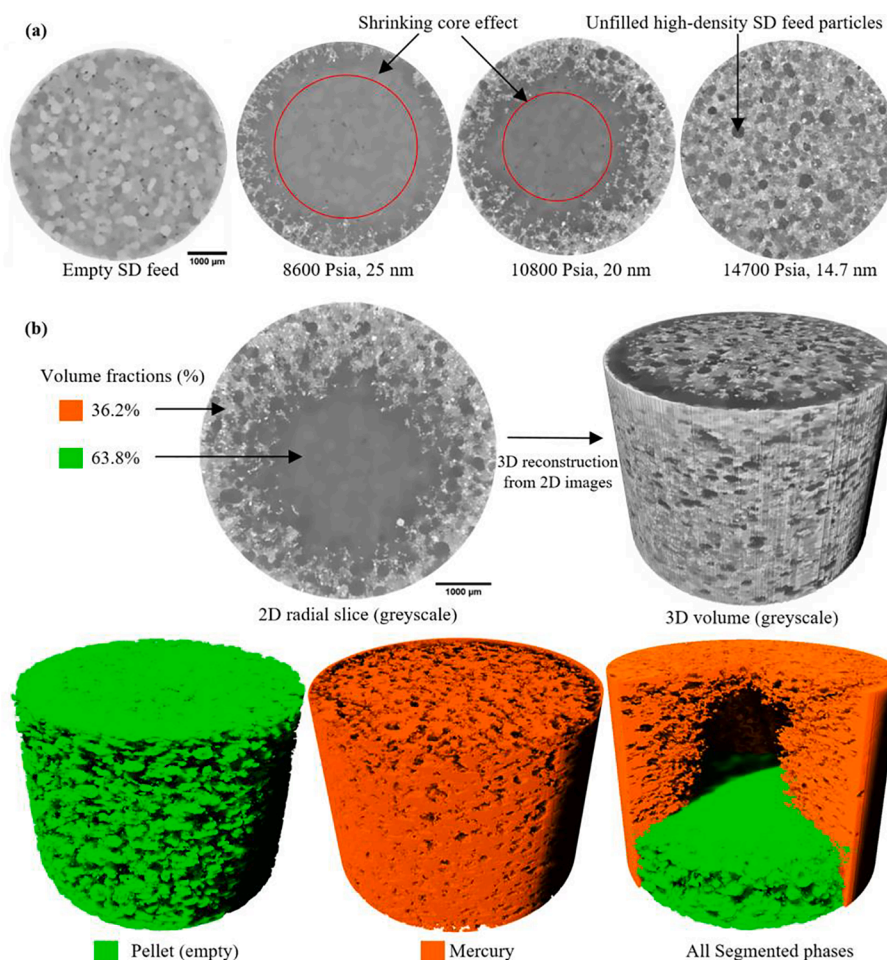


**Fig. 11.** (a) 2D radial slice CXT images of whole fresh spray dried pellet following mercury intrusion to a range of pressures. (b) Segmented 3D reconstruction CXT images of a partially mercury intruded fresh SD feed pellet up to 10,800 Psia. The scale bar corresponds to 1000  $\mu\text{m}$ .

In order to examine further the impact of the entrapped mercury, the variation of MTC with increasing mercury intrusion pressure was compared with that predicted for a random distribution of entrapped mercury calculated from the Prager [30] model, as described in previous work [6]. The comparison, of the observed fractional decline in the MTC following entrapment with that expected for the same mercury saturation, from the Prager [30] model, is shown in Fig. 17(a) and (b). From Fig. 17(a) and (b), it can be seen that, for both SD and RC feed pellets, the MTC is increasingly depressed below that expected for a random distribution of entrapped mercury following mercury intrusion to 10,800 psia and then 14,700 psia. However, for intrusion to the highest pressures ( $\geq 21,000$  psia), the then observed decline in MTC becomes the same as that expected for a random distribution of mercury. Fig. 17(a) and (b) also show the variation in adsorption-corrected MTC, for the SD and RC, with fraction of the pore volume occupied by water, and a comparison with that expected for a completely random arrangement of the blocking water phase, as predicted by the Prager [30] model. It can be seen that, for both SD and RC feed pellets, the MTC is much lower than would be expected for a random arrangement of water, thereby suggesting that, in an empty sample, the pores that subsequently are filled with water must have been making a significant, greater than expected, contribution to the mass transport.

## 5. Discussion

The combination of the CXT with rate of adsorption studies following mercury entrapment allows the determination of the identity of features

of the void space structure that are critical to mass transport. The rate of adsorption data for the SD and RC feed pellets showed that the MTC declined well below that expected, theoretically according to Prager [30] model, for a random distribution of mercury entrapped following intrusion to 10,800 and 14,700 psia. This suggests that the zones of the void space lost due to mercury entrapment following these intrusions are very important to mass transfer as their loss led to a greater than expected decline in MTC, relative to the benchmark random structure. From the CXT images of pellets following intrusion to these pressures, it can be seen, by eye, that the mercury is entrapped in a non-random pattern. In the case of the SD feed, the entrapped mercury advanced in a front towards the centre of the pellet, as amount entrapped increased with increased intrusion pressure. Given the barrier-like appearance of such a pattern of entrapment it seems clear why the loss of these pores is important. This pattern of entrapment implies that, when empty, there are pore pathways that, as they penetrate deeper into the pellet, are guarded by ever narrower necks. Hence, as diffusion penetration depth increases, the resistance to Knudsen diffusion will increase. In contrast, for the case of the RC feed pellet, mercury was entrapped in dendritic branches that traverse the pellet, thereby bypassing regions of high density. It is also clear that, for an empty pellet, these dendritic branches would provide diffusion pathways of lower resistance into the depths of the pellet. The slight increase in  $k/k_0$  for RC feed pellets between 14,700 and 20,200 psia is probably due to a decrease in the diffusion penetration depth,  $a$ , between these pressures, rather than a change in pore network diffusivity, as more mercury is entrapped. This rise in  $k/k_0$  is probably due to more mercury becoming



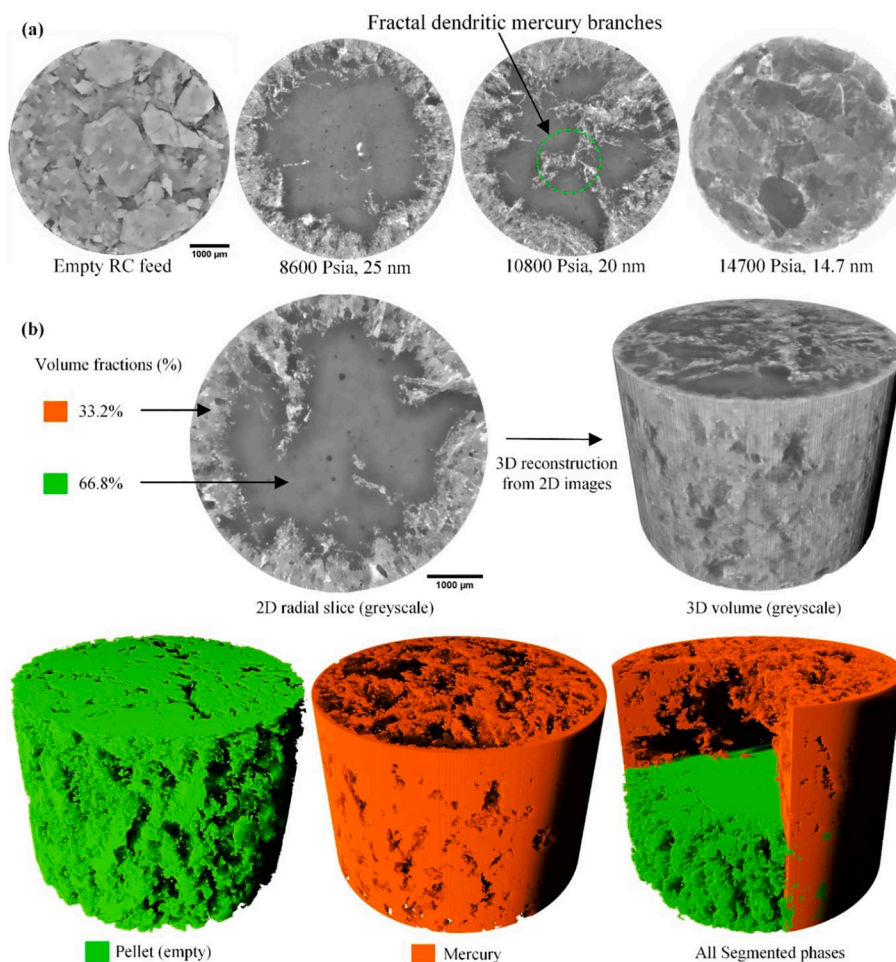


**Fig. 12.** (a) 2D radial slice CXT images of whole fresh roll compacted pellet following mercury intrusion to a range of pressures. (b) Segmented 3D reconstruction CXT images of a partially mercury intruded fresh RC feed pellet up to 8600 Psia. The scale bar corresponds to 1000  $\mu\text{m}$ .

entrapped in the core of the pellet as intrusion penetrates this region, thereby restricting gas uptake to only within the surrounding mantle region.

The multi-modal imaging at different resolutions aids the interpretation of the more indirect but multi-scale characterisation methods. This is shown schematically in Fig. 18. From Fig. 18, it can be seen that the additional, large pore size step in the mercury intrusion PSD for the SD feed particles is probably related to the 'bubble pores' seen in the high-resolution CXT images of the SD feed. The sizes in this step represent the pores in the shells that are seen to surround the bubble pores in the CXT images or the bubble pores more directly where this shell has been breached to the exterior. The gas overcondensation isotherms show these bubble pores are retained in the pellet made from the SD feed. This is because the typical size of many of the bubble pores, as seen in the higher resolution CXT images, of  $\sim 10\text{--}100\ \mu\text{m}$  is too large to achieve condensation during the conventional gas adsorption experiment. Hence, the gap between the top of the conventional adsorption isotherm and the overcondensation curve for the empty pellet is probably due to the existence of the bubble pores. The relative sharp desorption knee, at high relative pressures, that only arises in the overcondensation, and not the conventional, desorption probably represents the pore-blocking due to the smaller pores in the shells around the bubble pores. The bubble pores seen in the higher resolution CXT images are probably also responsible for the bright white dots seen in the lower-resolution CXT images of SD feed pellets following mercury entrapment. The distinct, circular, white dots are probably mercury that has become entrapped within the bubble pores. It is noted that some

lower resolution CXT images even show white circular dots within darker round SD feed particles that have not been (much) intruded with mercury. This suggests that, while the shell of bubble pores near the margins of the individual SD feed particles is readily penetrated, the rest of the SD feed particle is shielded by narrower necks and thus is not penetrated at that pressure.

It has been seen that, for both types of pellet, the decreasing accessibility of the pore network due to mercury entrapment was made manifest in the overcondensation isotherms via the widening in the hysteresis with the conventional adsorption isotherms. However, this hysteresis widening arose from very different patterns in the spatial distribution of entrapped mercury in the two types of pellet, as seen in the lower resolution CXT images. In the case of the RC feed the higher resolution CXT images have revealed the fractal structure of the RC pellets. It is known [31] that fractal structures tend to lead to fractal processes within them. In this case the penetration pathways during quasi-equilibrium imbibition of mercury into the RC feed pellet are also fractal.

It has been found that the second, lower pressure, more rounded percolation knee, seen in the overcondensation desorption isotherm for the SD feed pellets, has also been retained in the OC curve for the fragmented SD feed pellets (given in the [Supplementary Material](#)). This suggests that this knee is mostly associated with the accessibility of the individual SD feed particles, since the powder particle sizes are of the same size or larger than the feed particles in the lower resolution CXT images. The lower (amount adsorbed) convergence point for the overcondensation and conventional desorption isotherms for the fragmented

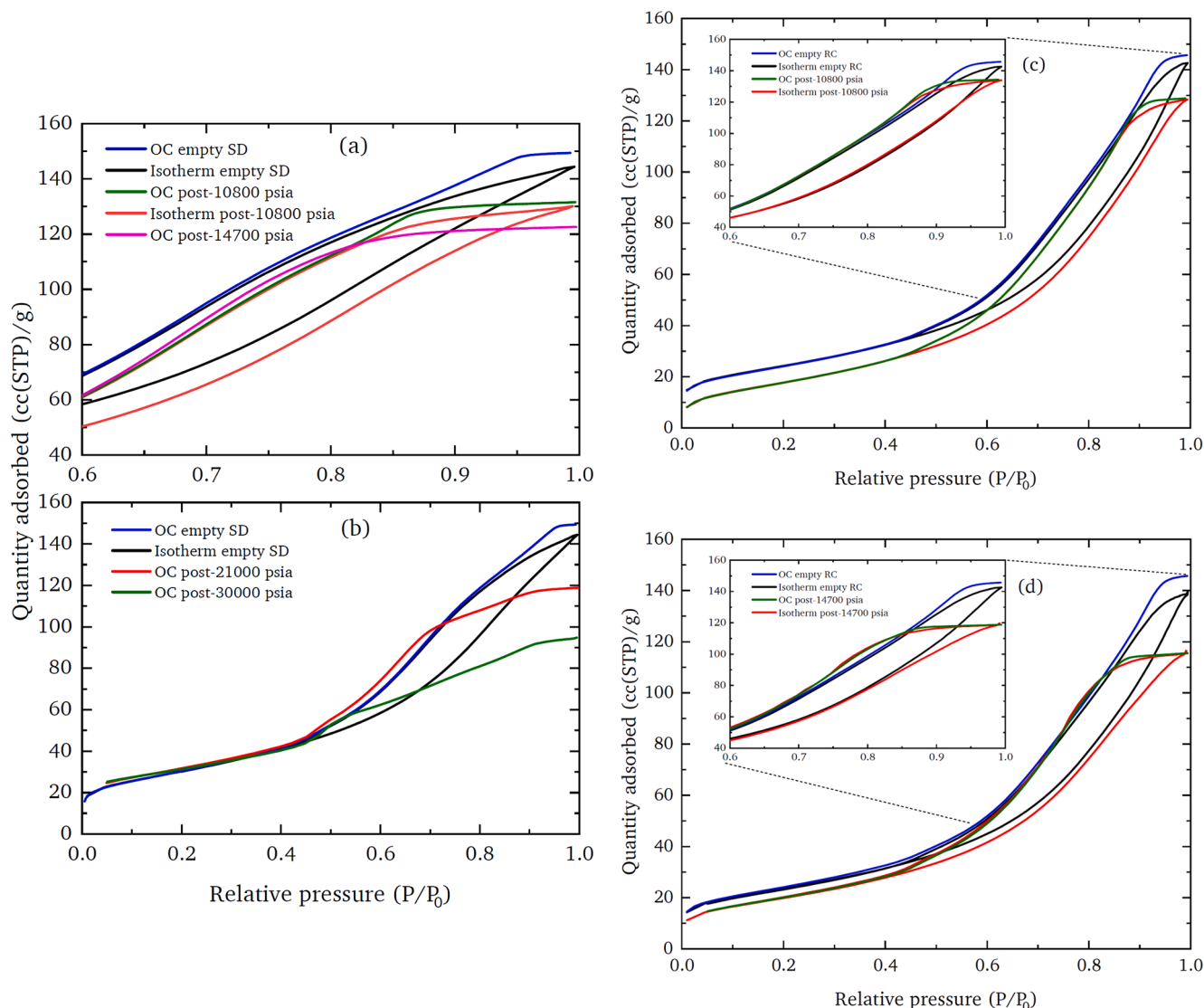


**Fig. 13.** (a) Upper part of hysteresis loop region of conventional sorption isotherms for empty SD feed pellet sample and SD sample following mercury intrusion to 10,800 psia, together with overcondensation boundary desorption isotherms for empty SD sample, and SD samples following mercury intrusion to 10,800 and 14,700 psia. (b) Hysteresis loop region of conventional sorption isotherms for empty SD feed pellet sample and overcondensation boundary desorption isotherms for empty SD sample, and SD samples following mercury intrusion to 21,000 and 30,000 psia. (c) Conventional sorption isotherms and overcondensation boundary desorption isotherms for empty RC feed pellet sample, together with conventional sorption isotherms and overcondensation boundary desorption isotherms for RC samples following mercury intrusion to 10,800 psia. The inset shows the isotherms obtained after mercury entrapment adjusted upwards by 5.5 cc(STP)/g. (d) Conventional sorption isotherms and overcondensation boundary desorption isotherms for RC samples following mercury intrusion to 14,700 psia. The inset shows the isotherms obtained after mercury entrapment adjusted upwards by 3.3 cc(STP)/g. (e) Conventional sorption isotherms and overcondensation boundary desorption isotherms for empty RC feed pellet sample, together with conventional sorption isotherms and overcondensation boundary desorption isotherms for RC samples following mercury intrusion to 30,000 psia.

pellet compared to the corresponding whole pellet data is due to the lower accessibility to vapour phase for some of the SD feed particles buried within the whole pellet, when compared with the fragmented pellet. The difference in the BJH adsorption PSDs between whole and fragmented pellets shows that, in some places, the cascade of pore filling during individual advanced condensation events spans length-scales larger than the powder particle size of 53–75  $\mu\text{m}$ , and thus probably encompasses more than one SD feed particle. Since there is an upper limit (of  $\sim 2$  from classical theory [2]) on the critical ratio of adjacent pore sizes to enable advanced condensation to proceed, then this suggests given SD feed particles must, themselves, be adjacent to particles with similar (i.e., within the critical ratio) pore sizes in at least one direction. This is consistent with the segregated lower resolution CXT

images that suggested that the low- and high-density tails of the distribution within SD feed particles are well-mixed, so the low density and high-density phases were each generally contiguous, and SD feed particles had neighbours of the same phase. This probably thus also explains why accessibility of the pellet interior to gas is maintained (as MTC value drops) despite the enveloping intrusion front seen in lower resolution CXT images of SD feed pellets following entrapment, albeit the open connections are only maintained by high density, lower pore size, SD feed particles.

The presence of advanced condensation effects, detected by comparing the adsorption PSDs for both whole and fragmented pellets (given in the [Supplementary Material](#)), suggests that disordered porous materials are not just composites of the pore structures of the unit cells

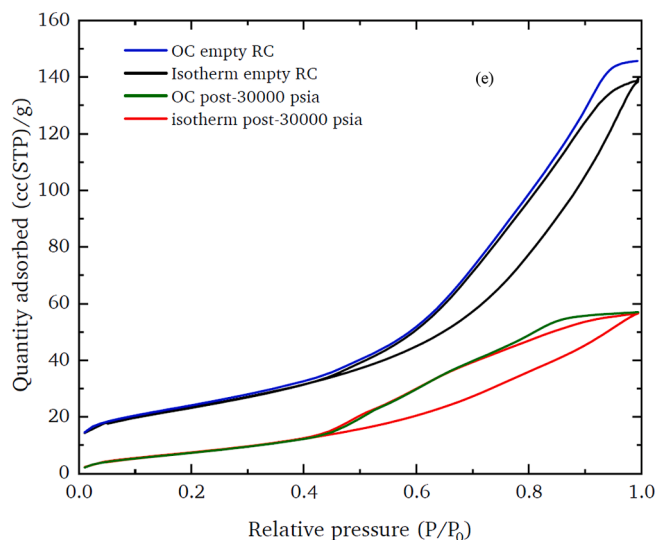


Fig. 13. (continued).

Table 5

Connectivity (Z) and lattice size (L) parameters from percolation analysis (Seaton [22]) of gas sorption data for (a) Fresh SD pellets and (b) Fresh RC pellets following mercury intrusion to different stated pressures.

Sample	(a) Fresh SD			(b) Fresh RC		
	Empty Pore fraction (%)	Z	L	Empty Pore fraction (%)	Z	L
Powder (53–75 $\mu\text{m}$ )	100.0	3.19	2.89	100.0	3.03	2.99
Whole pellet	100.0	2.98	3.07	100.0	2.95	3.01
Whole post 8600 psia	88.5	2.69	3.55	89.0	2.72	3.2
Whole post 10,800 psia	83.8	2.55	4.31	85.0	2.83	3.16
Whole post 14,700 psia	73.8	2.37	5.45	81.0	2.72	3.55

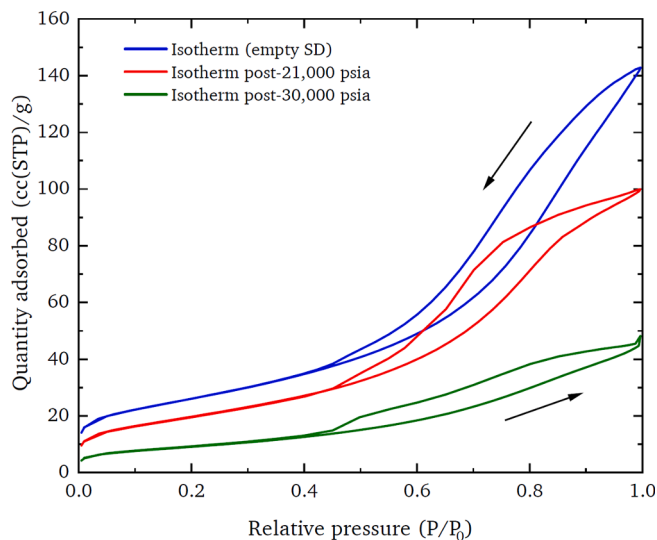


Fig. 14. Comparison of the conventional nitrogen sorption isotherms for the empty SD feed pellet, with the equivalent data following mercury intrusion to 21,000 and 30,000 psia.

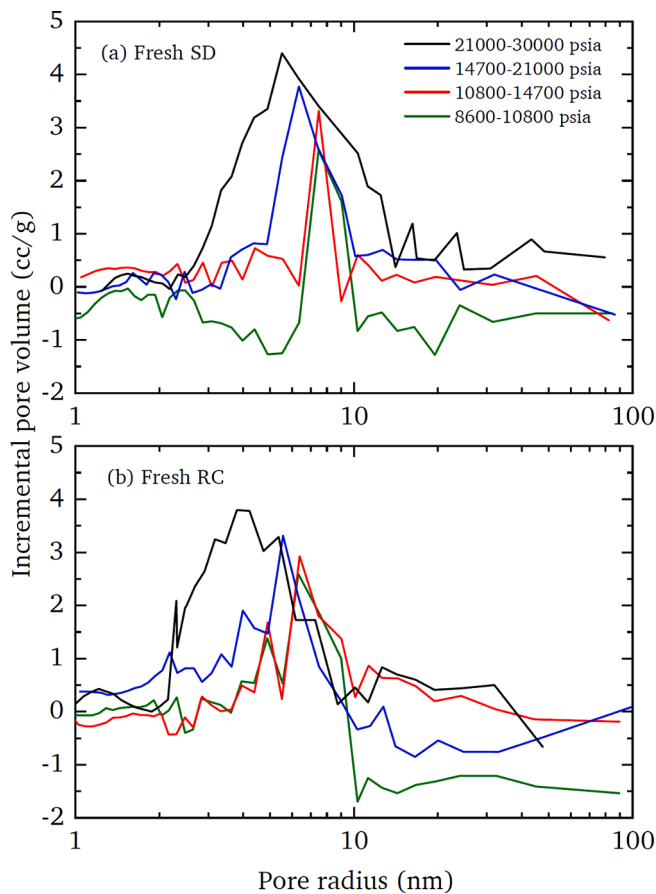
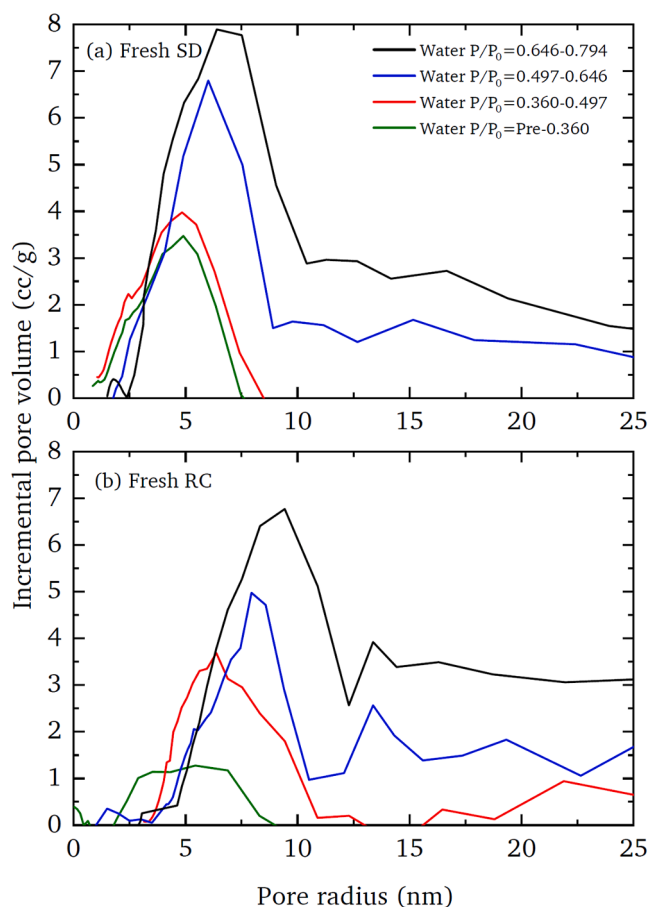


Fig. 15. BJH pore size distributions for the sub-sets of pores that become inaccessible from the exterior as the mercury intrusion pressure is increased to progressively higher ultimate pressures (as indicated in legend) for scanning curves. (a) Fresh SD, and (b) Fresh RC.

of templated, or otherwise controlled, pore size materials. The shift in the adsorption isotherm on fragmentation of the pellets shows that the juxtaposition of pore sizes over macroscopic scales is a critical feature of the overall porous structure. This suggests that the characteristic void space units for the capillary condensation process correspond to macroscopic regions of the network, rather than individual pores. The



**Fig. 16.** BJH pore size distributions for the sub-sets of pores that become inaccessible from the exterior as the water vapour pressure is increased to progressively higher pressures (as indicated in legend) for scanning curves. (a) Fresh SD, and (b) Fresh RC.

**Table 6**

Variation in adsorption-corrected MTC, for nitrogen at low pressure, with increasing mercury saturation for whole SD feed pellets.

MIP pressure /psia	Minimum pore diameter penetrated/nm	Fractional mercury saturation /%	Experimental $k/k_0$	Expected $k/k_0$ for random entrapment (Prager [30])
8,600	25.1	11.5	0.81	0.85
10,800	19.9	16.2	0.58	0.79
14,700	14.7	26.2	0.37	0.67
21,000	10.2	54.9	0.33	0.36
30,000	7.2	93.3	0.14	0.04

**Table 7**

Variation in adsorption-corrected MTC, for nitrogen at low pressure, with increasing mercury saturation for whole RC feed pellets.

MIP pressure /psia	Minimum pore diameter penetrated/nm	Fractional mercury saturation /%	Experimental $k/k_0$	Expected $k/k_0$ for random entrapment (Prager [30])
8,600	25.1	11.0	0.72	0.86
10,800	19.9	15.0	0.64	0.81
14,700	14.7	19.0	0.17	0.76
21,000	10.2	58.0	0.25	0.34
30,000	7.2	91.0	0.16	0.05

prevalence of network-scale, pore-to-pore co-operative effects in

disordered materials can only be determined by studying the material itself.

The succession of overcondensation isotherms, following progressively increasing levels of mercury entrapment, have shown that the boundary desorption isotherm from overcondensation experiments on empty SD feed pellets bridges between the micron-sized bubble pores, that do not fill with condensate in conventional sorption experiments, and the pore necks with sizes below 4 nm that would not be intruded by mercury. The gas sorption data obtained following mercury intrusion to 30,000 psia that shows the cavitation step also implies that these narrow necks are directly accessible from the exterior via pathways that do not include the pores filled with mercury, such as the bubble pores and low-density SD feed particles. They are thus probably located in, relatively unintruded, high density SD feed particles, as might be expected.

As discussed above, the studies of rate of adsorption for samples containing entrapped mercury have shown that some pores are more critical to mass transport than others. It is possible to define a pore utility index (PUI) that attempts to quantify the usefulness of a given pore size interval to overall mass transport, such that:

$$PUI = \frac{1 - \text{experimental } (k/k_0)}{1 - \text{expected } (k/k_0) \text{ for random structure}} \quad (11)$$

The PUI calculated for the SD and RC feed pellets from the ROA data in Tables 6 and 7 are shown in Fig. 19. It can be seen that the pore intervals of 15–11 and 20–15 nm have the highest PUIs for the RC and SD feed pellets, respectively.

A measure of the relative accessibility of particular pores to the exterior can be obtained from a relationship between the roundedness of the percolation knee of the overcondensation isotherm and the tortuosity for mass transport, as will be described here. Given that tortuosity is a measure of the extension of the path length of the diffusional flux beyond that of the straight-line distance across the porous medium, then the relative change in tortuosity ( $\Delta\tau = \tau - \tau_0$ ) can be related to the relative change in effective network size,  $\Lambda$ , such that:

$$\frac{\Delta\tau}{\tau} = \frac{\Delta\Lambda}{\Lambda} \quad (12)$$

since, if the effective size of the network is increased, then the path length of the diffusive flux will correspondingly be increased.

The apparent, effective size of the network will be increased if the size of the underlying model percolation lattice,  $L$ , is increased. The aforementioned CXT images of the pellets following mercury porosimetry, in Figs. 11–12, show that many feed particles remain free, or virtually free, of any entrapped mercury, while some others are completely, or nearly completely, filled with entrapped mercury. Hence, the individual feed particles tend to be either open or closed, respectively, following mercury porosimetry, and, thus, can be considered either present, or absent, respectively, from the model percolation network representing the macroscopic structure of the pellet. Therefore, the physical size of the underlying lattice unit in which  $L$  is measured can be considered as the size of a pellet feed particle,  $w$ . The characteristic physical size of the overall network would be proportional to the inverse of the surface-to-volume ratio  $(S/V)_t$  of the tableted pellet itself. The corresponding constant of proportionality would be a geometry factor characteristic of the shape of the pellet. The ratio of the geometry factors for the feed particles and whole pellet is denoted  $\gamma$ , and would be equal to unity if the feed particles and pellet had the same geometrical shape. Hence, the macroscopic tortuosity for mass uptake into the pellet is related to the change in the size of the percolation model lattice ( $\Delta L$ ) following mercury entrapment according to:

$$\frac{\tau_{a0}}{\tau_a} = 1 - \gamma(L - L_0)w \left( \frac{S}{V} \right)_t \quad (13)$$

Hence, for a given pellet type, the ratio of the original experimental tortuosity to the tortuosity measured following pore structural modification via mercury entrapment should be a linear function of the lattice



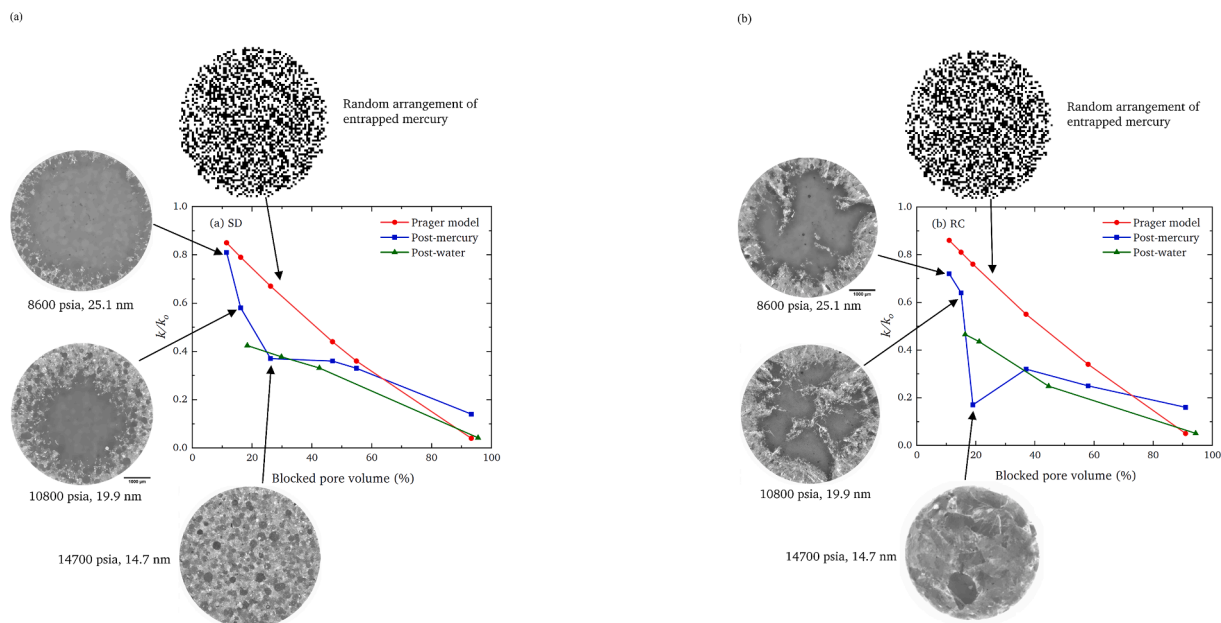


**Fig. 17.** Comparisons of the observed fractional decline in the mass transfer coefficient ( $k/k_0$ ) following mercury entrapment (■) and water adsorption (▲) and that expected for a random arrangement of entrapped of pore liquid from Prager [30] model (●) for (a) SD feed and (b) RC feed pellets. The pressures and pore sizes correspond to the ultimate values achieved in the mercury intrusion scanning curves.

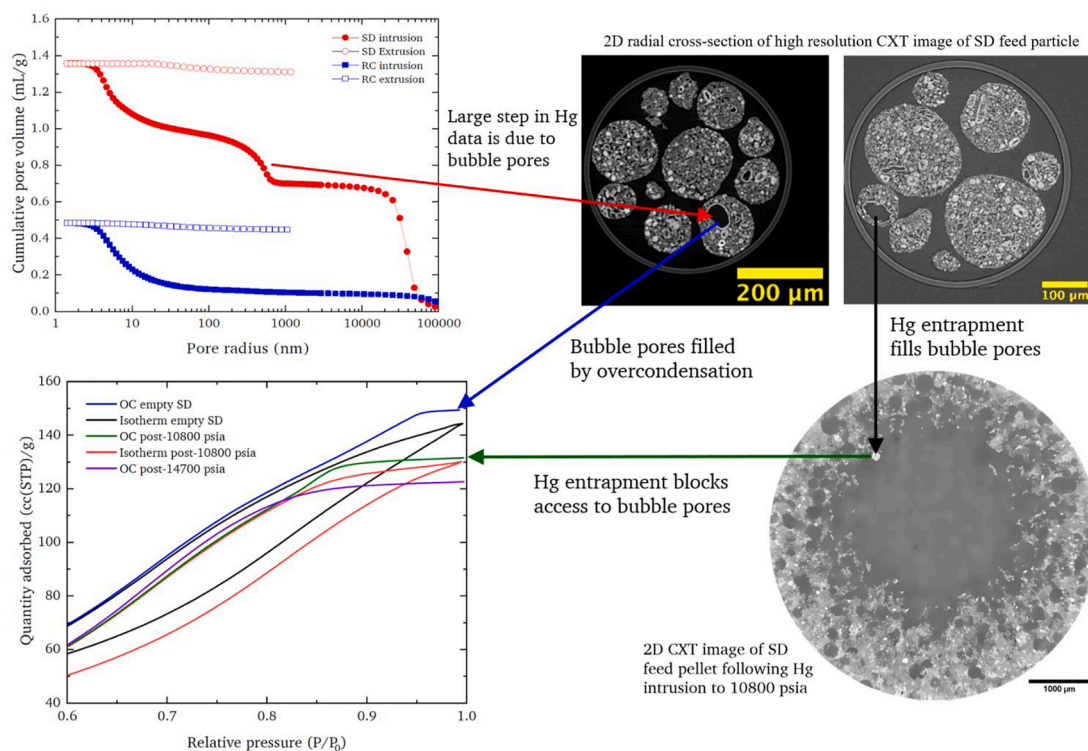


**Fig. 18.** Schematic diagram showing how features of the pellet macroscopic structure, seen in the CXT images, impact the indirect data characterising the porosity, and how gas sorption and mercury porosimetry data inform the interpretation of aspects of the images.

size obtained from percolation analysis of the corresponding over-  
condensation isotherm.

From the BJH difference PSDs in Fig. 15, it can be seen that, as mercury is entrapped over pressure intervals 8600–10800 and 10800–14700 psia, the position of the peak in the pore sizes being filled stays the same for both the SD and RC feed pellets, and so the critical pore size for mass transport will remain the same. The remaining

porosity following mercury entrapment is one minus the fractional mercury saturation given in Tables 6 and 7. Hence, Eq.(3) can be used to determine the ratio of tortuosities, since the critical reference Knudsen diffusivity is a constant over intrusion pressures up to 14,700 psia. Eq. (13) suggests that the tortuosity ratio will be a linear function of the percolation lattice size  $L$ , and, indeed, this is what is seen for both SD and RC feed pellets in Fig. 20.

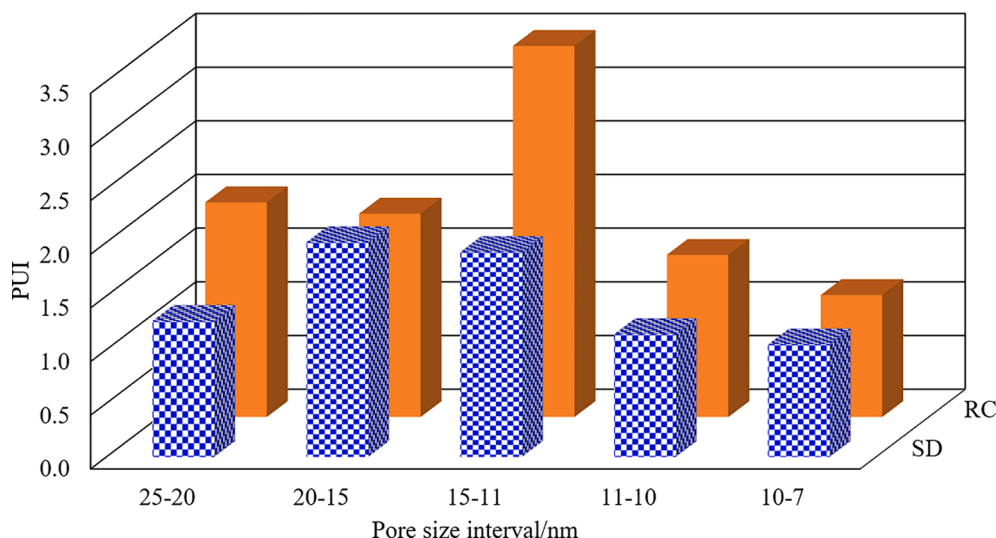


Fig. 19. Measures of usefulness, to mass transport in SD and RC feed pellets, of pore size intervals, as indicated by PUI.

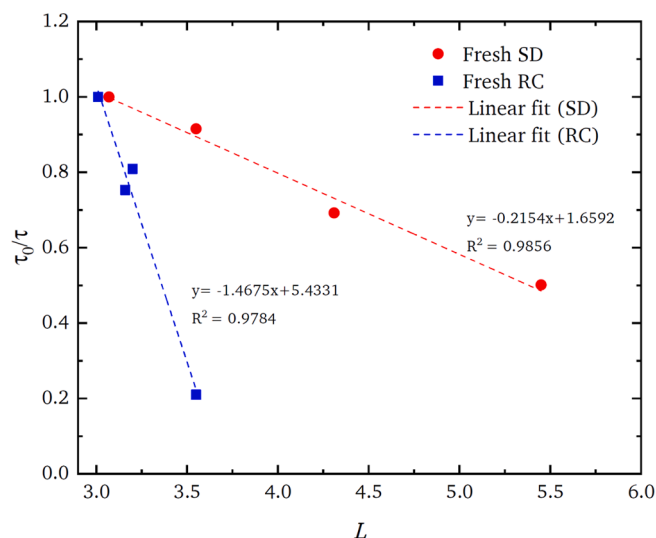


Fig. 20. A plot of the tortuosity ratio (from Eq. (3)) against percolation lattice size (from Table 5) for SD (red●) and RC (blue■) feed pellets following mercury entrapment to different intrusion pressures.

A universal plot for both pellet feed types can be obtained by plotting the data for each according to Eq.(13) using the surface-to-volume ratio of the pellets calculated using the dimensions given in Table 2, and taking typical feed particle sizes of 200 and 1300  $\mu\text{m}$  for the SD and RC feed particles. From Fig. 21, it can be seen that the experimental data give rise to a good fit to Eq. (13). The best-fit values for typical feed particle sizes from Eq.(13) are consistent with what is observed in the CXT images of pellets, as seen from the similarity in grid size divisions and feed particle sizes in the images given in Supplementary Material Figure A9, and could be confirmed by directly measuring feed particle sizes in the CXT images, and the average values thereby obtained for SD and RC feed were 205 and 1290  $\mu\text{m}$ , respectively.

The good fit of Eq.(13) to the experimental data suggests that the macroscopic structure of the pellets is well-represented by a random bond network percolation lattice, where the feed particles relate to the individual lattice bonds. Hence, the percolation behaviour of the pellets is dominated by the macroscopic structural heterogeneities resulting from heterogeneity in the feed particles. The key difference in the pellet fabrication route relevant to mass transport is manifested in the different

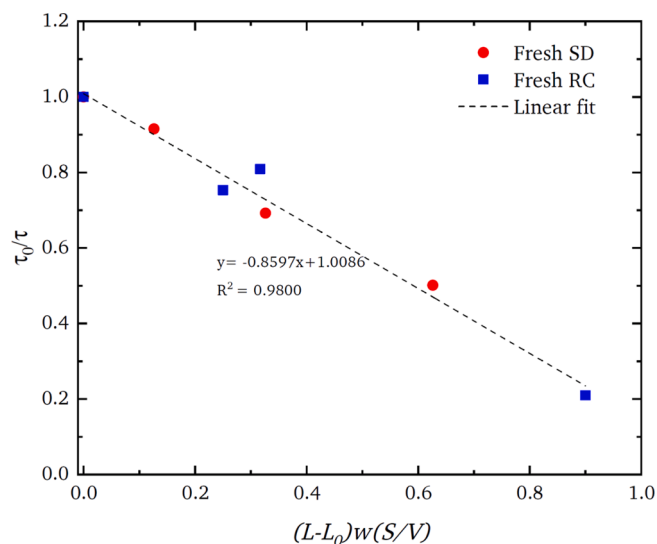


Fig. 21. Plot of Eq.(13) for experimental data for SD (red●) and RC (blue■) feed pellets.

values of the parameter  $w$  in Eq. (13), which corresponds to the feed particle size for the tableting process.

The reason that the key parameter of the model of macroscopic structure is the lattice size is that this parameter is a measure of the prevalence of surface clusters of larger pores important in an invasion percolation process like gas desorption or mercury intrusion. The roundedness of the percolation knee in gas desorption or mercury intrusion represents 'premature' penetration of the invading phase before the critical pressure for sample-spanning percolation is reached. In a completely random structure, the probability of formation of surface clusters is enhanced by the larger surface area-to-volume ratio of smaller lattices raising the probability of a given pore being located on the surface. When using a random lattice to represent a real heterogeneous material, an apparent small model lattice size represents a greater propensity for surface clusters than for a random structure. For example, the 'shrinking core' effect evident in the spatial pattern of the progressively encroaching front of entrapped mercury in the CXT images of the SD feed pellets reveals the particular creation of surface clusters of mercury penetration in this material. This is reflected in the steep growth in apparent model lattice size for this material as entrapped mercury fills

up the surface clusters of larger pores with increasing intrusion pressure, so they are no longer available to facilitate nitrogen desorption. The abstract model lattice size is thus a measure of the prevalence of surface clusters of larger pores, with apparently smaller random lattice sizes indicating higher prevalence. These surface clusters of larger pores provide 'super-highways' giving easier and shorter paths to access the pellet interior for diffusing gas, and thus, when lacking for an apparently larger lattice size, mass transport is associated with higher tortuosity. The CXT images of partially mercury-intruded RC feed pellets show that the actual, real surface clusters in this type of pellet have a very different geometric form to those of the SD feed pellet. However, the results in Fig. 21 show that they both can be 'mapped' onto the surface clusters of an equivalent random pore bond network lattice, where the apparent lattice size of the virtual network is a proxy 'measure' of the relative incidence and penetration depth of the real surface clusters of particular pore size ranges. The coupled pore-sifting and percolation modelling procedure used here can successfully abstract the key aspect needed (to predict mass transport) from the otherwise apparently intractable, high degree of complexity of the real pellet structures revealed in the CXT and FIB-SEM images.

## 6. Conclusion

The above findings have shown how combining indirect characterisation methods, such as overcondensation and mercury porosimetry, that can bridge several orders of magnitude in pore size, even down to molecular scale, with imaging methods that can provide detailed spatial information but for limited range of resolution and/or field-of-view, can lead to a much more comprehensive and inter-linked characterisation of disordered hierarchical porous media. The hybrid characterisation methods, integrating several techniques in one overall experiment, ensures that the characterisation data from different methods coheres and produces synergistic findings. The combination of overcondensation with multi-scale imaging identified the macropore structures missing from conventional isotherm data, namely the large 'bubble pores', and also allowed the specific sizes of the smaller pores shielding these structures to be measured.

It has been seen that the 'filtering' or 'sifting' strategy, involving combining characterisation techniques, described here can identify and spatially-locate the particular pore sizes that most control mass transport in pore structures of different character arising from different fabrication methods. As a result, different pore size intervals can be allocated a pore utility index value that quantifies their relative usefulness to mass transport. The characterisation methods also allow indication of how particular pore structural features relate to raw material properties and fabrication method. Hence, the impact of the choices made in catalyst pellet manufacturing on mass transport can be identified and quantified.

It has been shown that a random pore bond network is a successful model for the macroscopic heterogeneity in pellet structure, as characterised by the percolation parameters, especially apparent lattice size. The percolation theory-based analysis of the overcondensation data has successfully, quantitatively predicted the relative change in tortuosity, from rate of adsorption experiments, as successively more of the pore structure is filled with entrapped mercury, thereby increasing the apparent lattice size. The model has demonstrated that the degree of heterogeneity in average pore sizes amongst individual feed particles, and their particle size relative to that of the pellet itself, greatly impacts the accessibility of the pellet interior. While it has been seen that surface clusters of larger pores control access to the interior for both feed types, their particular geometric form has its origins in the feed type and fabrication process of the pellet. The differential importance, for mass transport, of particular pore size ranges within these surface clusters for each pellet-type has been evaluated, and their location within the pellets has been visualised.

## Declaration of Competing Interest

The authors declare that they have no known competing financial interests or personal relationships that could have appeared to influence the work reported in this paper.

## Data availability

The data that has been used is confidential.

## Acknowledgements

This work was supported by the Engineering and Physical Sciences Research Council [grant number EP/R512059/1]. VN acknowledges funding from the European Union's Horizon 2020 research and innovation programme under the Marie Skłodowska-Curie Grant Agreement No 701647. We acknowledge the Paul Scherrer Institut, Villigen, Switzerland, for providing synchrotron radiation beamtime at the TOMCAT beamline X02DA of the SLS. SM and SPR thank Dr. C. Parmenter of the University of Nottingham nmRC for the FIB-SEM work.

## Appendix A. Supplementary data

Supplementary data to this article can be found online at <https://doi.org/10.1016/j.cej.2022.139122>.

## References

- [1] M.V. Twigg, *The Catalyst Handbook*, second ed., CRC Press, Taylor & Francis Group, Boca Raton, FL, 2014.
- [2] S.P. Rigby, *Structural Characterisation of Natural and Industrial Porous Materials: A Manual*, Springer International Publishing: Cham., 2020.
- [3] M. Arif, M. Mahmoud, Y. Zhang, S. Iglaier, X-ray tomography imaging of shale microstructures: A review in the context of multiscale correlative imaging, *Int. J. Coal Geol.* 233 (2020), 103641.
- [4] L. Ma, P.J. Dowe, E. Rutter, K.G. Taylor, P.D. Lee PD, A novel upscaling procedure for characterising heterogeneous shale porosity from nanometer-to millimetre-scale in 3D, *Energy* 181 (2019) 1285–1297.
- [5] D.A.M. de Winter, F. Meirer, B.M. Weckhuysen, FIB-SEM Tomography Probes the Mesoscale Pore Space of an Individual Catalytic Cracking Particle, *ACS Catal.* 6 (5) (2016) 3158–3167.
- [6] A. Nepryahin, R.S. Fletcher, E.M. Holt, S.P. Rigby, Structure-transport relationships in disordered solids using integrated rate of gas sorption and mercury porosimetry, *Chem. Eng. Sci.* 152 (2016) 663–673.
- [7] J. Yao, W. Song, D. Wang, H. Sun, Y. Li, Multi-scale pore network modelling of fluid mass transfer in nano-micro porous media, *Int. J. Heat Mass Trans.* 141 (2019) 156–167.
- [8] W. Song, J. Yao, K. Zhang, H. Sun, Y. Yang, The impacts of pore structure and relative humidity on gas transport in shale: A numerical study by the image-based multi-scale pore network model, *Transp. Porous Media* (2021), <https://doi.org/10.1007/s11242-021-01663-6>.
- [9] G.D. Cody, A. Davis, Direct imaging of coal pore space accessible to liquid metal, *Energy Fuels* 5 (1991) 776–781.
- [10] J. Kaufmann, Pore space analysis of cement-based materials by combined Nitrogen sorption - Wood's metal impregnation and multi-cycle mercury intrusion, *Cem. Concr. Compos.* 32 (2010) 514–522.
- [11] L. Ruffino, R. Mann, R. Oldman, E.H. Stitt, E. Boller, P. Cloetens, M. DiMichiel, J. Merino, Using x-ray microtomography for characterisation of catalyst particle pore structure, *Can. J. Chem. Eng.* 83 (2005) 132–139.
- [12] A. Nepryahin, R.S. Fletcher, E.M. Holt, S.P. Rigby, Techniques for direct experimental evaluation of structure-transport relationships in disordered porous solids, *Adsorption* 22 (7) (2016) 993–1000.
- [13] F. Hill-Casey, T. Hotchkiss, K.A. Hardstone, I. Hitchcock, V. Novak, C.M. Schlepütz, T. Meersmann, G.E. Pavlovskaya, S.P. Rigby, Hyperpolarised xenon MRI and time-resolved X-ray computed tomography studies of structure-transport relationships in hierarchical porous media, *Chem. Eng. J.* 405 (2021), 126750.
- [14] C. Rieckmann, F.J. Keil, Simulation and experiment of multicomponent diffusion and reaction in three-dimensional networks, *Chem. Engng Sci.* 54 (1999) 3485–3493.
- [15] S. Gheorghiu, M.-O. Coppens, Optimal bimodal pore networks for heterogeneous catalysis, *AIChE J.* 50 (4) (2004) 812–820.
- [16] B.C. Bukowski, F.J. Keil, P.I. Ravikovitch, et al., Connecting theory and simulation with experiment for the study of diffusion in nanoporous solids, *Adsorption* 27 (2021) 683–760.
- [17] J. Rouquerol, G.V. Baron, R. Denoyel, H. Giesche, J. Groen, P. Klobes, P. Levitz, A. V. Neimark, S. Rigby, R. Skudas, K. Sing, M. Thommes, K. Unger, Liquid intrusion

- and alternative methods for the characterization of macroporous materials (IUPAC Technical Report), *Pure Appl. Chem.* 84 (2012) 107–136.
- [18] A.V. Neimark, P.I. Ravikovitch, Capillary condensation in MMS and pore structure characterization, *Micropor. Mesopor. Mat.* 44–45 (2001) 697–707.
- [19] J. Jagiello, A. Chojnacka, S.E.M. Pourhosseini, Z. Wang, F. Beguin, dual shape pore model to analyze the gas adsorption data of hierarchical micro-mesoporous carbons, *Carbon* 178 (2021) 113–124.
- [20] S.P. Rigby, L.F. Gladden, The Use of Magnetic Resonance Images in the Simulation of Diffusion in Porous Catalyst Support Pellets, *J. Catal.* 173 (1998) 484–489.
- [21] S.P. Rigby, L.F. Gladden, NMR and fractal modelling studies of transport in porous media, *Chem. Eng. Sci.* 51 (1996) 2263–2272.
- [22] N.A. Seaton, Determination of the connectivity of porous solids from nitrogen sorption measurements, *Chem. Eng. Sci.* 46 (1991) 1895–1909.
- [23] S.P. Rigby, M.J. Watt-Smith, R.S. Fletcher, Simultaneous determination of the pore-length distribution and pore connectivity for porous catalyst supports using integrated nitrogen sorption and mercury porosimetry, *J. Catal.* 227 (2004) 68–76.
- [24] S. Kirkpatrick, In R. Balian, R. Mayward, G. Toulouse (Eds.), *Ill-Condensed Matter*, North-Holland, Amsterdam (1979), p. 321.
- [25] J. Kloubek, Hysteresis in porosimetry, *Powder Technol.* 29 (1) (1981) 63–73.
- [26] S.P. Rigby, L. Stevens, T. Meersmann, G.E. Pavloskaya, G.J. Rees, J. Henderson, S. J. Bryant, K.J. Edler, R.S. Fletcher, Structural and chemical heterogeneity in ancient glass probed using gas overcondensation, X-ray tomography, and solid-state NMR, *Mater. Charact.* 167 (2020), 110467.
- [27] K.L. Murray, N.A. Seaton, M.A. Day, An Adsorption-Based Method for the Characterization of Pore Networks Containing Both Mesopores and Macropores, *Langmuir* 15 (1999) 6728–6737.
- [28] D. Paganin, S.C. Mayo, T.E. Gureyev, P.R. Miller, S.W. Wilkins, Simultaneous phase and amplitude extraction from a single defocused image of a homogeneous object, *J. Microsc.* 206 (1) (2002) 33–40.
- [29] F. Marone, M. Stampanoni, Regridding reconstruction algorithm for real time tomographic imaging, *J. Synchrotron Radiat.* 19 (6) (2012) 1029–1037.
- [30] S. Prager, Diffusion in inhomogeneous media, *J. Chem. Phys.* 33 (1) (1960) 122–127.
- [31] D. Avnir, *The Fractal Approach to Heterogeneous Chemistry*, Wiley, New York, 1989.